Department of Physics and Astronomy

University of Heidelberg

Master thesis

in Physics

submitted by

Meike Danisch

born in Herford

2014

Scintillation light detection in XENON1T:

Photosensor tests and light collection simulations

This Master thesis has been carried out by Meike Danisch

at the

Max Planck Institute for Nuclear Physics

under the supervision of

Prof. Dr. Manfred Lindner

Scintillation light detection in XENON1T:
Photosensor tests and light collection simulations

The experiment XENON1T aims at directly detecting dark matter via interactions of weakly interacting massive particles (WIMPs) with xenon nuclei. The goal of XENON1T is to improve the sensitivity compared to its predecessor experiment XENON100 by 2 orders of magnitude by using a larger xenon volume and by reducing the amount of background events. The XENON1T inner detector, which contains 2.2 t of liquid xenon, will be equipped with 248 photomultiplier tubes (PMTs) to detect the scintillation light induced by a possible WIMP interaction. For this purpose 3″ R11410-21 PMTs with low intrinsic radioactivity and high quantum efficiency are being manufactured by Hamamatsu. One part of this thesis describes the tests of the first 90 R11410-21 PMTs. Important features like the dark count rate and the gain were measured at room- and liquid xenon temperature. The second part of this thesis is dedicated to investigating the scintillation light propagation and the light collection efficiency (LCE) in a XENON1T-like detector. A Monte Carlo simulation based on GEANT4 was developed to test how different assignments of quantum efficiency (QE) values to the PMT positions affect the LCE. In a first approach, it is found that optimizing the PMT arrangement, considering the QE values, can enhance the LCE value by a factor of $\approx 7\,\%$ at most, which would result in a $\approx 7\,\%$ higher light yield for XENON1T.

Detektion von Szintillationslicht im Experiment XENON1T:
Tests der Lichtsensoren und Simulationen der Lichtausbeute

Das Experiment XENON1T sucht nach dunkler Materie in Form von schwach wechselwirkenden, schweren Teilchen (WIMPs), indem mögliche Wechselwirkungen der WIMPs mit den Xenon Atomkernen im Detektor nachgewiesen werden sollen. Gegenüber dem Vorgänger-Experiment XENON100 soll mit XENON1T, durch Vergrößerung des Xenon Volumens und Reduzierung der störenden Untergrundsignale, eine 100-mal bessere Sensitivität erreicht werden. Das Innerste des Detektors enthält 2.2 t flüssiges Xenon und wird mit 248 Photoelektronenvervielfachern (PMTs) ausgestattet um das Szintillationslicht zu detektieren, welches in möglichen Wechselwirkungen der WIMPs mit dem Detektor entsteht. Hierfür werden 3″ R11410-21 PMTs mit besonders niedriger intrinsischer Radioaktivität und hoher Quanteneffizienz durch Hamamatsu produziert. Der erste Teil dieser Arbeit beschreibt die Tests, die mit den ersten 90 dieser PMTs durchgeführt wurden. Im zweiten Teil dieser Arbeit geht es um die Simulation der Ausbreitung des Szintillationslichtes und der Lichtausbeute (LCE) in einem XENON1T ähnlichen Detektor. Mit Hilfe einer Monte Carlo Simulation basierend auf GEANT4 wurde untersucht, wie sich unterschiedliche Anordnungen der PMTs, bezüglich ihrer Quanteneffizienz, auf die LCE auswirken. In einem ersten Ansatz wurde eine optimale PMT Anordnung für XENON1T entwickelt und es konnte gezeigt werden, dass mit dieser der LCE Wert, und somit auch die Lichtausbeute maximal um einen Faktor von $\approx 7\,\%$ verbessert werden kann.

Contents

Chapter 1

Introduction

To motivate the search for dark matter, in the first part of this introduction three main questions will be shortly discussed: Why do we need dark matter, what is it and how can it be detected? The second part is devoted to the details of dark matter detection in the experiment XENON1T. For experiments like XENON1T and also for this thesis photomultiplier tubes play a fundamental role and thus their functionality and some of their properties will be outlined in the third and last part of this chapter.

1.1 Dark matter

The astronomer Jan Oort was the first one to coin the term "dark matter" in 1932 in connection with the discrepancy between luminous and gravitationally interacting matter [1]. One year later Fritz Zwicky proposed that the dark matter in the universe might not be simply dim or hidden stars, like Oort had suspected, but a new and unknown form of matter [2], which does not show electromagnetic interactions with common matter.

In the 60's Vera Rubin started to study the rotation curves of spiral galaxies like the Milky Way [3] and the unexpected result is up to now a very convincing hint to the existence of dark matter. A rotation curve is the plot of the circular velocity v of objects in a galaxy versus their distance r from the galactic center. The visible mass component of a spiral galaxy can approximately be described by a solid, rotating disk. According to Newtonian mechanics, such a disk shows a linear rise of velocities for small radii according to the relation $v = \omega \cdot r$ and a Keplerian decline $v \propto r^{-1/2}$ for larger distances from the center. The dashed curve in Fig. 1.1 shows the just described, expected behavior of a rotation curve. One can also see the measured rotational velocity of the galaxy NGC 6503. It shows an unexpected behavior: after the velocity reaches its maximum, it is flat for increasing distances, even beyond the radius of the visible galaxy. The absence of the expected decline of rotational velocities has been observed for many other spiral galaxies, too [3] [4]. Assuming Newtonian mechanics, which states

$$v(r) = \sqrt{\frac{G \cdot M(r)}{r}}\,, \tag{1.1}$$

where $M(r)$ is the mass content at the radius r and G the gravitational constant, the aforementioned observation implies that these galaxies must have an additional, invisible component, with its mass content increasing linearly with radius. Fig. 1.1 shows that a model, including a dark matter halo around the galaxy in addition to the visible objects and gas, fits the measured data very well.

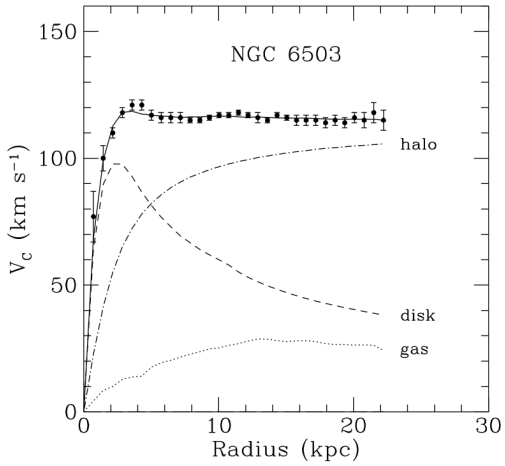

Figure 1.1: *Rotation curve of the galaxy NGC 6503. Data points and a fit with contributions from a luminous disk, gas and a dark matter halo with a density profile of an isothermal sphere [4].*

An alternative approach, proposed by M. Milgrom in 1983, is to modify Newtonian dynamics on extragalactic scales [5]. But this so-called MOND scheme is only able to explain the rotation curves of spiral galaxies correctly [6], but not the other anomalies which are described in the following.

In the first decade of the 21st century, after the Chandra X-ray observatory witnessed, amongst others, the merging galaxy cluster E065756 ("bullet cluster") [7], Markevitch et al. combined those measurements with optical and weak lensing observations [8]. The result is shown in Fig. 1.2. The overall matter region, reconstructed by analyzing the gravitational

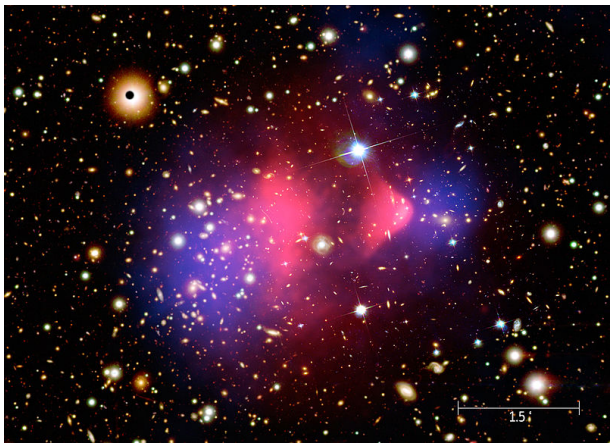

Figure 1.2: *X-ray, optical and weak gravitational lensing observations of the merging galaxy cluster E065756 ("bullet cluster") [8] [9].*

lensing is colored blue. The X-ray emitting plasma is the main contribution to the baryonic mass and is colored in red. The fact that overall matter and baryonic matter regions have a $8\,\sigma$ significance offset was interpreted as "direct empirical proof of the existence of dark matter" [10] and explained in the following way. During the collision of galaxies the baryonic matter is slowed down by electromagnetic interactions. But this cannot happen to dark matter which can easier pass by the other galaxy and thus moves ahead.

Even if there are many hints to the existence of dark matter, it is still unclear what it is actually made of. Possible baryonic constituents could be so called MACHOs (Massive compact halo object) [11]. These astronomical objects, including for example neutron stars and brown dwarfs, emit little or no radiation, which makes them hard to detect. MACHOs have been searched for by means of gravitational microlensing [12], but not enough of these objects have been found to make up the Milky Way's dark matter halo mass. The non-baryonic candidates are elementary particles that can be subdivided into cold and hot dark matter. The attribute hot means that the particle had a relativistic velocity at the age of the universe when galaxies could just start to form. The attribute cold means that the particle was moving at non-relativistic speed [13]. But there is a problem with hot dark matter, whose most prominent candidate is the neutrino. It is not obvious, how structures like stars, galaxies and clusters emerged from the universe, when it was about 400000 years old. Therefore, the formation of large-scale structures under different conditions has been simulated, for example by Springel et al. [14]. They found that only in case of the existence of cold dark matter, the simulation yields reasonable results. If the dark matter was hot, structures of today's universe could not have emerged. The most popular non-baryonic, cold dark matter candidates are WIMPs - weakly interacting massive particles - with masses in the range of a few GeV to a few TeV. An important argument for the WIMP is that the predicted relic dark matter density, fixed by the freeze-out in the early universe, is of the same order of magnitude as the observed density, if one assumes weak-scale interactions. WIMP candidates appear in different theories beyond the standard model of particle physics. One example is the lightest neutralino arising in supersymmetric theories [13].

The cosmic microwave background (CMB) allows insight into the universe at the time when it became transparent to photons, because the continuously interacting plasma consisting of electrons, protons and photons became neutral due the formation of hydrogen. Measurements of the CMB anisotropies can provide information on the amount of dark matter in the universe. Recent measurements, performed by the Planck satellite, indicate that the energy of the universe is made up of only 4.9 % baryonic matter, 26.8 % dark matter and 68.3 % dark energy [15], as predicted by the ΛCDM model [16], which can be seen as the standard model of cosmology. Here, CDM stands for cold dark matter and Λ is the cosmological constant.

But how can the WIMP be detected? There are in general three approaches. First, there is the indirect detection method. If one assumes that the WIMP is it's own antiparticle, which is the case for the neutralino, two of them can annihilate producing for example a quark and an antiquark, a lepton and an antilepton, two W bosons or two Z bosons [16]. These particles can again decay into secondary particles like γ-rays, neutrinos, positrons and electrons or protons and antiprotons, reaching the earth from space. γ-rays can be detected by means of γ-ray telescopes like the Large Area Telescope (LAT) on the Fermi satellite or Cherenkov telescopes like VERITAS, MAGIC or the planned Cherenkov Telescope Array (CTA). Experiments like SuperKamiokande or IceCube look for WIMP annihilations via neutrinos. Magnetic spectrometers like PAMELA or AMS-02 on the International Space Station (ISS) can detect charged particles and their antiparticles. A possible dark matter signature would be an excess of positrons or anti-protons over the astrophysical backgrounds.

The second approach uses the fact that in particle colliders like the Large Hadron Collider (LHC) dark matter particles could be produced. One possible signature is the pair-production of WIMPs with initial or final state radiation [16]. Another possibility is to use events with pair production of strongly interacting particles, because they are much more likely, and while the products decay, a WIMP could be produced and detected via missing transversal energy.

The third approach is to try and detect WIMPS directly via interactions with the target material in a dedicated dark matter detector. It seems that the WIMP does neither interact

electromagnetically nor via the strong force, thus direct detection experiments must rely on possible weak-scale interactions with ordinary matter. The WIMPS, that cross the earth with a flux of about $10^5\,\mathrm{cm}^{-2}\,\mathrm{s}^{-1}$ [6], will also cross the dark matter detectors and those heavy, neutral particles could elastically scatter off the target nuclei [17]. In this way, the dark matter particles deposit energy indirectly, via recoiling nuclei, in the detector. The aim of the direct detection experiments is to measure the differential event rate $^{dR}/_{dE_r}$ where E_r is the recoil energy of the nucleus that was hit. This event rate depends, amongst astrophysical assumptions, on the both unknown WIMP mass and WIMP-nucleus cross section. It can be distinguished between a spin dependent part, which scales with $J(J+1)$, where J is the nuclear spin, and a spin independent part, which scales with A^2, where A is the atomic number [6]. Both parts of course depend on the unknown WIMP-nucleon, or even more fundamentally speaking, the WIMP-quark interaction strength and the exchange particle that is involved in the process. The dependency of the differential event rate on the recoil energy is illustrated in Fig. 1.3 for different WIMP masses. It shows an exponential dependency, which becomes

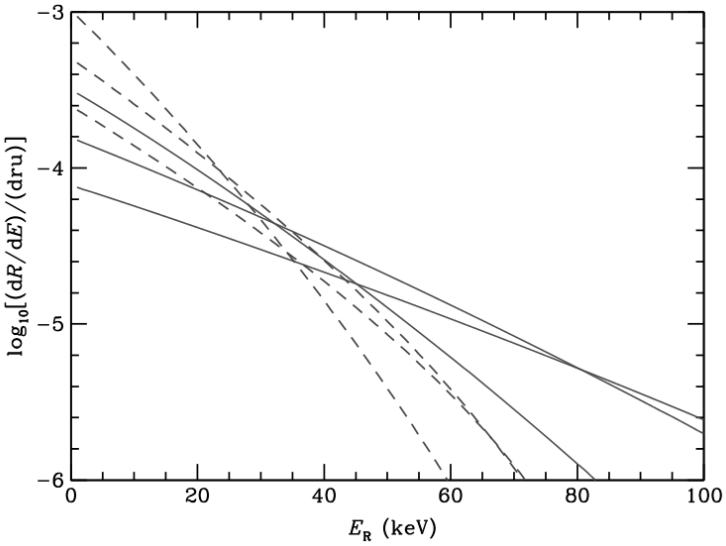

Figure 1.3: *Spin independant differential event rate (in dru = counts per kg, day and keV) of a direct detection experiment using Xe (dashed lines) and Ge (solid lines), for WIMP masses of 50, 100 and 200 GeV (from bottom to top at $E_R = 0\,\mathrm{keV}$). A WIMP-proton cross section of 10^{-8} pb is assumed for this plot [6].*

steeper for decreasing WIMP mass. If the measured WIMP interaction rate does not exceed the background rate, the respective experiment can at least give limits on the cross section for a range of WIMP masses.

Depending on the instrumented detector material, one or a combination of three measures of deposited energy are being used: scintillation light, ionization charge and heat. Reading out more than one form of energy can give additional information on the type of interaction and thus on the incoming particle (this is explained for the combination of light and charge in Section 1.2).

Only scintillation light is being read out for example by DAMA which uses NaI(Tl) crystals as a target. This experiment found an annual modulation [18] of the scintillation signal [19]. Since the earth orbits the sun, while the sun moves around the galactic center and thus through the dark matter halo, the relative velocity of the earth through the halo is larger when the velocities of the sun and the earth are added up and smaller when the two velocities are

subtracted for the other half of the year. Therefore, the WIMP flux on earth would fluctuate annually and so would the dark matter interaction rate in the detector. Analyzing an exposure of 1.33 tonne-year, DAMA found an oscillating signal at 9.3 σ C.L. [20]. The ionization channel only is used for example by the experiment CoGeNT, utilizing germanium detectors, which also found an annual modulation signal [21]. The combinations of possible WIMP masses and cross sections derived from the DAMA and CoGeNT results are shown in Fig. 1.4. This plot reveals, that the results are not compatible if there is only one WIMP mass and cross section.

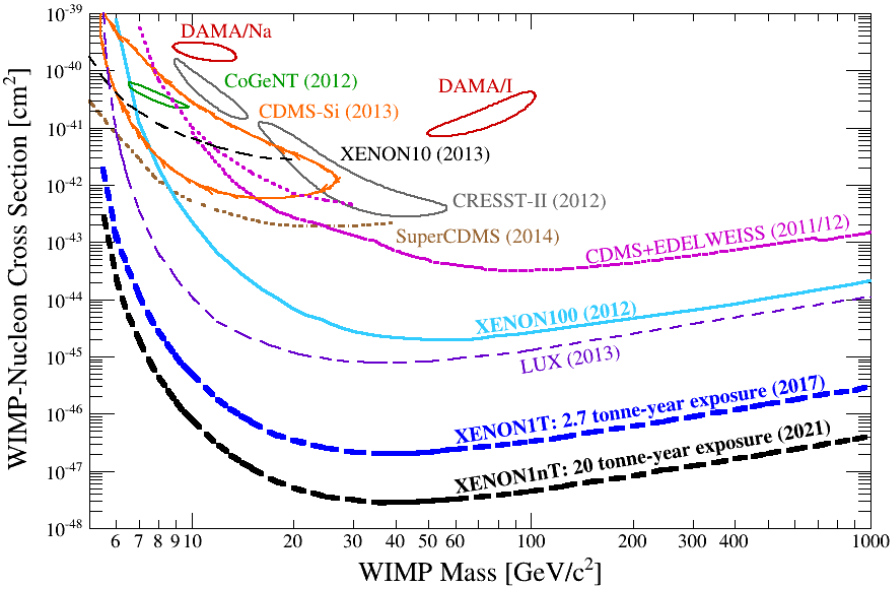

Figure 1.4: *Current limits on the spin-independent WIMP-nucleon cross section from XENON100, LUX, EDELWEISS and CDMS, results from DAMA, CoGeNT, CDMS and CRESST and predicted limits for the future XENON1T experiment after two years of operation in 2017 and for the planned upgrade XENONnT in 2021 [22].*

Experiments like XENON [23] and LUX [24] use the liquid noble gas xenon as detector material. Since xenon is a good scintillator and ionizer in response to incoming particles (see [6] Chapter 21), both channels are being used. Neither LUX nor XENON has found a significant signal yet and thus these experiments rule out all dark matter detection signals that have been published up to now. In 2013, LUX published their limit on the spin-independent WIMP-nucleon cross section, which makes LUX the most sensitive dark matter experiment at the moment (see Fig. 1.4). Fig. 1.4 also shows the predicted sensitivity for XENON1T, which is the successor experiment of XENON100 and is at the moment under construction at the Gran Sasso underground laboratory (LNGS [25]) in Italy. The desired sensitivity will be reached for example by exposing 1 t of liquid xenon (LXe) for 2.7 years, which is predicted for 2017 and will probe new cross sections for all considered WIMP masses.

Experiments like CDMS [26], CRESST [27] or EDELWEISS [28] measure the little temperature changes when a particle hits a crystal held at very low temperatures in the range of mK. CDMS and EDELWEISS use germanium (CDMS additional silicon) crystals, and both also measure the ionization charge signal in addition to the released heat. CRESST on the other hand uses $CaWO_4$ crystals, which are also used as scintillators. Both CDMS as well as CRESST found significantly more events than the background expectation in Si-crystals [29] and $CaWO_4$ crystals, respectively. CDMS and EDELWEISS set limits on the WIMP-nucleon

cross section using the non-observation of unexpected events in the employed Ge-crystals. Fig. 1.4 shows that SuperCDMS sets at the moment the most stringent limit on cross sections for low WIMP masses [30].

1.2 The XENON1T dark matter experiment

The XENON experiments aim to directly detect dark matter via interactions of WIMPs with xenon nuclei and the goal of XENON1T is to improve the sensitivity on the spin-independent WIMP-nucleon cross section, compared to its predecessor experiment XENON100, by 2 orders of magnitude within two years of operation [31], as shown in Fig. 1.4. This can be achieved by increasing the xenon target volume by a factor of ten and by reducing background events per unit mass, measurement time and energy range by two orders of magnitude.

The XENON1T inner detector is a so-called time projection chamber (TPC). It will be placed in a cryostat and both will be filled with an overall amount of about 3 t liquid xenon. The TPC itself will contain about 2.2 t liquid xenon, the so-called target or active volume, and a layer of gaseous xenon (GXe) on top of it. The inside of the TPC will be optically separated from the outside by PTFE (Teflon) panels, because Teflon has a very high reflectivity for UV light. Fig. 1.5 shows a schematic drawing which illustrates the operation principle of such a two-phase TPC. When an incoming particle meets a xenon atom, the interaction can

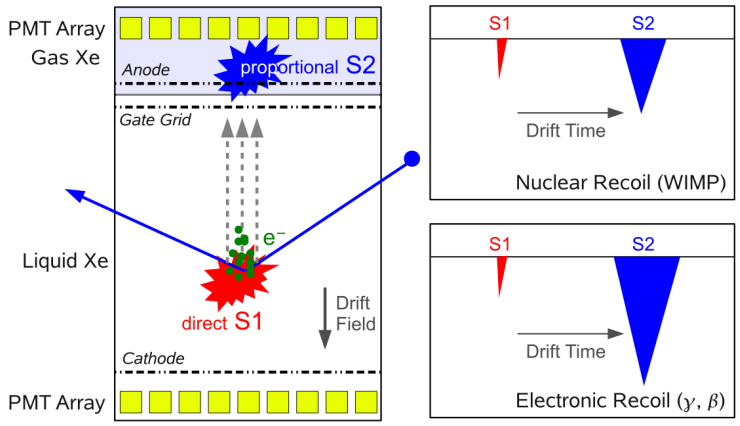

Figure 1.5: *Left: Sketch of a two-phase TPC with liquid xenon and gaseous xenon volumes, bottom and top photomultiplier tube arrays and three electrode grids [23]. Right: Background discrimination method via the signal amplitude ratio.*

be classified into two scenarios: electronic and nuclear recoil. In case the incident particle is a γ-ray or electron, it interacts mostly with the orbital electrons (electronic recoil). In the other case, if the incoming particle is neutral and heavy like the WIMP or a neutron, it elastically scatters off the xenon nucleus. As a result, the recoiling atom scatters off the surrounding xenon atoms (nuclear recoil). In both cases, excited xenon atoms (excitons), ion-electron pairs and heat are produced, but the relative amount is different in the two scenarios. The excitons and the ion-electron pairs can de-excite and recombine, respectively, producing scintillation light, with a wavelength of 178 nm, which is immediately detected by several of the overall 248 photomultiplier tubes. This added up prompt scintillation signal is called $S1$. The electrons originating from ionized xenon atoms are accelerated by the electric drift field towards the top of the TPC where they are extracted to the gaseous xenon layer by a stronger electric field between the gate grid and the anode (see Fig. 1.5). As a next step, these

further accelerated electrons interact with xenon atoms and produce a number of scintillation photons which is proportional to the number of ionization electrons reaching the gas phase. This proportional scintillation light [32] is again detected by several PMTs and the summed up signal is called $S2$. This sequence of pulses contains various information, like deposited energy and 3D position of the event. From the time difference between the $S1$ and $S2$ pulse, using the drift velocity caused by the electric field strength, one can calculate the vertical i.e. z-position of the interaction. The horizontal i.e. x- and y-position of the event can be reconstructed from the pattern of how the $S2$ signal is distributed over the top PMTs. The resulting 3D position of the interaction can be determined with a resolution of the order of mm and it is mainly used to reject events near the TPC walls, which are very likely background events [23]. The remaining volume where events are valid is called fiducial volume and will cover a cylinder, 1 m high and 1 m in diameter, containing about 1 t of LXe in XENON1T [31]. Another way to reject background events is by distinguishing electronic and nuclear recoil events. Due to the different ratio of produced excitons and ion-electron pairs, the two also show a different ratio of $S1$ and $S2$ signal amplitude (see Fig. 1.5). This makes neutrons the most disturbing background particles because they cannot be distinguished from WIMPS by means of this method.

Neutrons can be generated in (α, n)-reactions following radioactive α-decay, also due to spontaneous fission or spallation of nuclei by muons. Electrons can occur in form of β-radiation and γ-rays arise as a byproduct in all radioactive decays. Ionizing radiation can come from the outside of the experiment, originating for example from the uranium and thorium content of the surrounding rocks. But this background can be shielded easier than the radioactive contaminations in the TPC materials like the PMTs for example. The most dangerous source of radioactivity are contaminations inside the LXe itself, because the resulting events cannot be eliminated by defining a fiducial volume. This includes ^{85}Kr, which is naturally contained in xenon and ^{222}Rn, which can emanate from the TPC materials into the xenon volume. Another distracting background source for experiments searching for rare processes are muons, originating from cosmic rays. Muons can either directly interact with the active xenon volume or, by interaction with the detector materials, produce cosmogenic radionuclides, resulting in radioactivity in turn. To reduce the muon flux, XENON1T is located underground. The Gran Sasso rock, which has an average height of 1400 m above the LNGS, reduces the muon flux by 6 orders of magnitude. The outermost layer of the experiment, the water tank shown in Fig. 1.6, has already been built at the time of writing. It will be filled so that 4 m of water shield the inner detector all around from neutrons and γ-rays coming from the outside [31]. The tank also serves as muon veto since it will be equipped with photomultiplier tubes detecting Cherenkov light induced by muons crossing the water. This way, events that might be caused by a muon can be rejected [33]. To keep the level of contamination in LXe low, a purification system is needed.

One important part of the experiment is the energy calibration, because it is necessary to reconstruct the recoil energy, which a WIMP might deposit in the detector, from the measured PMT signals $S1$ and $S2$. For this purpose radioactive sources emitting γ-rays with well known energies are placed close to the detector. Per keV deposited energy, ξ scintillation photons and ζ ionization electrons are produced, where ξ stands for the scintillation yield and ζ for the ionization yield. The percentage of photons that is lost due to e.g. photon absorption in LXe, limited reflectivity of the Teflon walls and limited efficiency of the PMTs is called light collection efficiency (LCE). The number of detected $S1$ photons per keV of deposited energy, which combines ξ and LCE, is the so called light yield

$$LY = LCE \cdot \xi \,. \tag{1.2}$$

Figure 1.6: *Sketch of the XENON1T experiment [22]. Left: Hall B at LNGS, where XENON1T is being constructed at the time of writing. Right: The water tank with the two-phase xenon TPC inside.*

When this quantity is measured by means of calibration, one can use it to calculate any, via electronic recoil deposited, energy from the $S1$ signal. In case of energy deposition via nuclear recoil, one needs a conversion factor to calculate the recoil energy. This is the so called effective scintillation yield L_{eff}, which is a function of the recoil energy and has to be be determined experimentally.

1.3 Basic principles about photomultiplier tubes

The photomultiplier tube is a very popular device, which is used in many physics experiments to detect light. A PMT can measure light at very low intensities and is able to count even single photons.

Fig. 1.7 is a schematic drawing of a PMT, showing basically an evacuated tube with a photocathode, a focusing grid, several dynodes and an anode, all held at different voltages by means of a voltage divider circuit, in this most simple example consisting of several resistors.

The photon detection principle is the following. When light strikes the photocathode through the entrance window, each photon can cause the emission of an electron due to the photoelectric effect with the probability η, referred to as quantum efficiency. These electrons, called photoelectrons (PE), are accelerated in the direction of the first dynode by means of the potential difference between the cathode and the first dynode. The probability that an electron actually reaches the first dynode is called collection efficiency α and is enhanced by the focusing grid. Hitting the first dynode, each photoelectron produces a certain number of secondary electrons by striking out some of the the atoms' orbital electrons in the dynode material. This number of secondary electrons is called multiplication factor δ. The voltages applied to the dynodes are chosen in such a way that the initial and secondary electrons travel to the second dynode where every electron again knocks out electrons and this process is repeated until all electrons reach the anode. The probability that an electron follows the intended way from one dynode to another we call p. In general, the geometries between two dynodes do not have to be equal. Therefore, the probability p can be different for each stage. Also, the voltage differences between two dynodes are not always chosen equally, by choosing non-equal resistances for the voltage divider circuit. Larger voltage differences between two

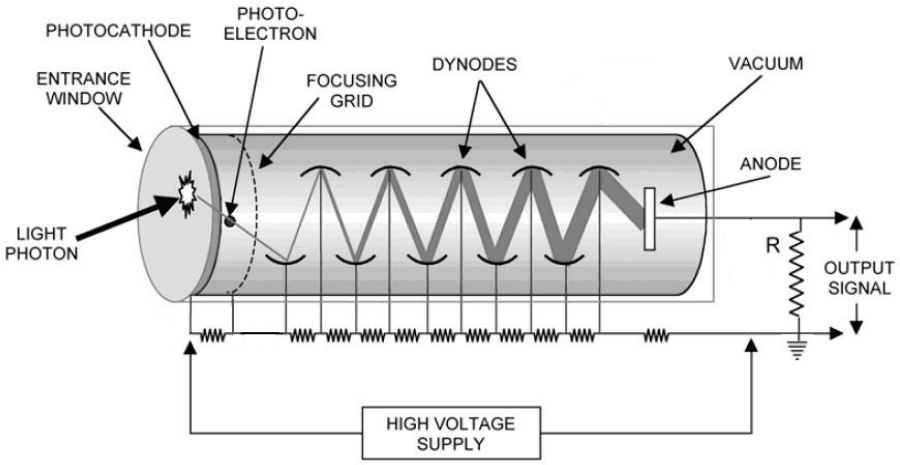

Figure 1.7: *Schematic drawing of a PMT with a connected voltage divider circuit, high voltage supply and signal readout.*

dynodes lead to higher kinetic energies of the electrons, resulting in larger multiplication factors

$$\delta_i = a \cdot (U_i)^k \quad \forall i \in \{1, \ldots, n\}, \tag{1.3}$$

where a is a constant and U_i is the voltage between two dynodes. The quantity k describes a constant property of the dynode material [34] and n is the number of dynodes, which is typically of the order of ten. As a result, for m photons striking the photocathode, the number of electrons that reach the anode is

$$m \cdot \eta \cdot \alpha \cdot \prod_{i=1}^{n} p_i \cdot \delta_i. \tag{1.4}$$

The quantity

$$\prod_{i=1}^{n} p_i \cdot \delta_i = g \tag{1.5}$$

is called gain. It is a very important property of a photomultiplier and can reach values up to 10^7. This property allows for a well detectable signal, without further amplification.

Inserting Equation 1.3 into Equation 1.5 one can calculate the dependency of the gain on the operating voltage U. For this purpose it is used that the voltage between two dynodes is proportional to the operating voltage:

$$U_i = \frac{R_i}{R_{\text{sum}}} \cdot U, \tag{1.6}$$

where R_i is the resistance between the two dynodes and R_{sum} the sum of all resistances (compare Fig. 1.7). As a result, the gain can be parametrized as follows:

$$g(U) = A \cdot U^{k \cdot n}, \tag{1.7}$$

where A is a function of the constants a, k, the number of dynodes n, the probabilities p_i and the resistances R_i.

One option to operate a PMT is to ground the anode and set the cathode to a negative potential. In this case, the charge at the anode flows off to ground over a resistance (see Fig. 1.7) for a certain period of time, resulting in a voltage pulse that can be viewed on an oscilloscope. In Fig. 1.8 the amplitude, the rise- and fall time and the full width at half maximum (FWHM) of this anode output voltage pulse are defined.

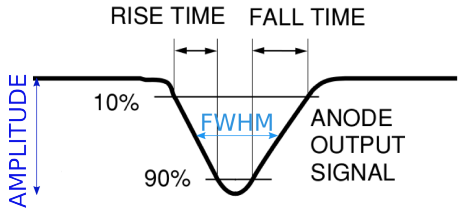

Figure 1.8: *The rise time of a PMT pulse is defined as the time needed for the signal to rise from* 10 % *to* 90 % *of its full amplitude. The fall time passes while the signal decreases again from* 90 % *to* 10 % *[34]. The quantity FWHM is the full width at half maximum.*

By integrating a PMT pulse, one receives the charge that reached the anode. This charge is proportional to the number of incoming photons m (see Equation 1.4). Therefore, the charge of a pulse is a measure of the incoming light intensity and is usually given in units of PE, which refers to the number of photoelectrons that reached the first dynode. The light intensity is the quantity of interest in many practical applications. If the PMT is used for scintillation light detection for example, the number of scintillation photons is a measure of the energy that was deposited in the scintillation medium by some particle.

The above-mentioned linearity between charge and number of incoming photons, as well as between the pulse amplitude and the light intensity, is another important feature of a PMT. It can saturate at very high photon intensities because on one hand, space charges at the dynodes or the anode can distort the electric fields and thus cause electrons to not follow their provided path. On the other hand, if the dynodes cannot be filled up with enough electrons after the removal of a large amount of charge carriers before the next pulse, this can affect the linearity, too.

When operating a PMT without light exposure, the background pulses, called dark counts, become apparent. The main cause at room temperature is thermionic emission of electrons from the photocathode. These electrons are multiplied by the dynode chain and cause an output pulse at the anode. According to Richardson's Law, the temperature dependency of the dark current, i.e. dark counts per time, can be written as

$$I \propto T^{5/4} \cdot \mathrm{e}^{-W/k_B T}, \tag{1.8}$$

where T is the temperature of the photocathode and W the work function, which is the minimum thermal energy for an electron to leave the surface (see [34] and references therein). Because the work function of photocathode materials must be very small, thermionic emission can occur even at room temperature [34]. Dark counts can also have other causes, which all have in common that electrons are knocked out from the photocathode and these electrons cannot be distinguished from photon-induced electrons i.e. photoelectrons. Among these causes are the secondary particles of cosmic rays and particles generated by radioactivity in the PMT material or environment. Dark counts also occur if electrons are knocked out from a dynode instead of the photocathode, also due to one of the aforementioned reasons, but the resulting pulses are smaller because the electrons do not undergo the whole multiplication procedure.

For the XENON1T PMTs, the dark count rate at −100 °C, the LXe temperature they will be operated at, is particularly important. To reach the desired sensitivity, there must be less than one background event in two years in the fiducial volume of XENON1T, after applying all cuts, i.e. rejecting all events that are most likely background events, identified for example on the basis of the vertex position or the $S1/S2$ signal ratio. Another criterion is that the $S1$ signal must be detected by several PMTs simultaneously. This way, dark counts of single PMTs are rejected as well. But the higher the dark count rate is, the higher is the probability for an accidental coincidence i.e. for dark counts to occur in two PMTs simultaneously.

Another effect causing additional counts during light exposure, or dark counts as a secondary effect, is afterpulsing. Despite the vacuum inside of the PMT, there are always some residual gas atoms that a photoelectron can scatter off [34]. If the latter ionizes an atom, the generated positively charged ion is accelerated back to the photocathode where it knocks out electrons, just like photons do. This results in an additional pulse, time-correlated to the prior so-called main pulse. The time delay between the two pulses is of the order of 1 µs and depends on the mass of the ion. The afterpulse probability is defined as the probability, that one photoelectron leads to at least one afterpulse [35].

Afterpulses should not be confused with so-called late pulses. The latter occur if a photoelectron is backscattered off the first dynode without knocking out further electrons and moves part of the way back in direction of the cathode, until it is accelerated back to the first dynode. If it knocks out further electrons this time, those secondary electron will be multiplied in the same manner as those of regular pulses. The only difference is, that the resulting pulses have a time delay of typically 10 ns due to the additionally traveled distance of the photoelectron.

Chapter 2

Experimental setup

In this chapter the XENON1T photomultiplier tube model "Hamamatsu R11410" is presented. Photomultiplier tubes have been used in physics experiments for a long time, but the experiments' requirements change over time, making it necessary to develop new models with improved performance or characteristics. And even if every PMT model has certain specifications, arising from measurements carried out by the manufacturer, the customer has to elaborately test all additional features, which are important for the experiment, and maybe even cross check the values given by the specifications. In XENON1T, malfunctioning photosensors in the running experiment would be a serious incident, because they could not be exchanged without great effort. At the Max Planck Institute for Nuclear Physics in Heidelberg (MPIK), a facility for PMT tests at room temperature has been built for a former experiment and is now used for testing the XENON1T PMTs. This setup, as well as a cooling setup for tests at cryogenic temperatures is described in the second part of this chapter.

2.1 The Hamamatsu photomultiplier tube R11410

The company Hamamatsu Photonics developed the PMT labeled R11410 for dark matter detectors which have certain demands. Photosensors in the XENON experiments are immersed in gaseous and liquid xenon. Both are kept at a temperature around $-100\,°C$ and the gas pressure takes on a value around 2 atm [23]. Under these conditions, in addition to the electric field environment, stable operation of the photomultiplier tubes must be possible over several years. The long-term stability of the model R11410 in LXe and its functionality when exposed to external electric and magnetic fields were verified in [36] and [37]. Furthermore, in the experiment XENON100 the intrinsic radioactivity of the PMTs strongly contributed to the electronic recoil background [38], which shows that the materials of all PMT components must be selected carefully to achieve the lowest possible intrinsic radioactivity [36]. For this purpose, together with the XENON collaboration, Hamamatsu developed step by step different versions of this PMT for XENON1T, with changing materials. The new materials in every step were screened for radioactivity by means of the low background germanium gamma spectrometers Gator [39] and GeMPI [40] at LNGS. The latest PMT version, labeled R11410-21, will be used. At this point, 91 PMTs have been delivered by Hamamatsu and every single one has undergone the radioactivity screening at LNGS and the detailed tests at MPIK that will be described in the next chapter. The screening results have been analyzed and as a result, the nuclear recoil event rate due to radioactive contaminations in the PMTs is estimated to be 0.028 events per year in a fiducial volume corresponding to 1 t [38].

Fig. 2.1 shows the PMT body which is 114 mm long and made from "cobalt-free Kovar", which is a special alloy with a very low ^{60}Co content. ^{60}Co can be generated by cosmic rays via neutron activation of the ^{59}Co, which natural cobalt consists of to 100 %. The quartz window

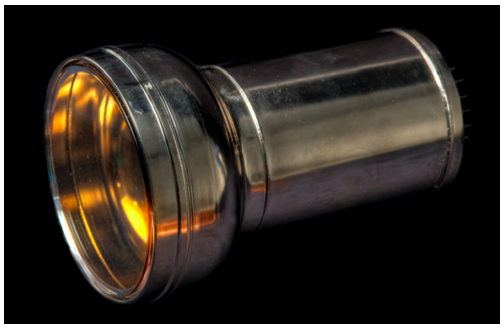

Figure 2.1: *Outside of the PMT R11410.*

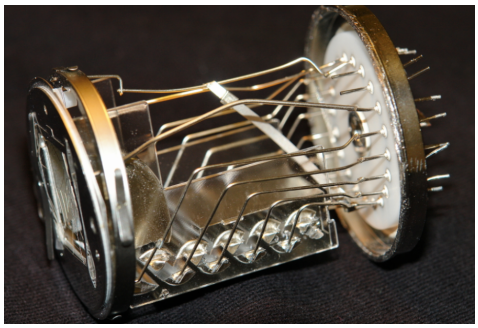

Figure 2.2: *Inside of the PMT R11410.*

has a diameter of 3″ or 76 mm, respectively. Quartz is a convenient window material because it is, in contrast to common glass, transparent for UV light. The photocathode material properties, like its work function, determine the quantum efficiency of a PMT, which also depends on the wavelength of the incoming light. The R11410 photocathode is made from so-called "bialkali", which allows for an exceptionally high quantum efficiency. It consists of different alkali metals (cesium and potassium) and antimony and is vapor-deposited to the window and the dynodes from the inside of a PMT [34]. The photosensor R11410 was designed to reach its maximum efficiency of typically $QE = 32.5\,\%$ at a wavelength of 178 nm, which corresponds to the wavelength of the LXe scintillation light. Note that the quantity QE is different from the quantum efficiency η introduced in Section 1.3, because it takes into account the reflectance R and absorption A of the entrance window:

$$QE = (1 - R - A) \cdot \eta \,. \tag{2.1}$$

The QE values were measured by Hamamatsu by comparing the PMT signal to that of a standard PMT (calibrated by means of a photodiode), when both are exposed to the same light intensity. The collection efficiency is typically $\approx 90\,\%$ [37].

Fig. 2.2 shows the inside of the PMT version at hand, fitting into the cylindrical part of the PMT body. From left to right, this figure shows the focusing grid, the first dynode, which is the largest one and placed right behind this grid, followed by 11 further dynodes and the anode. All of these electrodes are connected to little metal rods, which are fed through a ceramic stem to the outside of the PMT. The external parts of these rods, the leads, serve as electrical connectors. They have to be connected to a socket with a built-in voltage divider circuit, the so-called "base", which again is connected to the high voltage supply and readout electronics.

The base provides each electrode with a different voltage and creates the desired voltage gradient between the dynodes, like it is shown in Fig. 1.7. In XENON1T, the cathodes of the the R11410-21 PMTs are held at negative potential, typically around $-1500\,\mathrm{V}$ and the anode is grounded. The voltage divider, high voltage supply and signal readout circuit is shown in Fig. 2.3. This design was developed at the University of Zürich [41] with the aim of optimizing linearity, minimizing power dissipation and using materials with the lowest possible intrinsic radioactivity. The material components were screened to check for radioactivity at MPIK. The design was used to built bases at MPIK, which are utilized for testing the PMTs and the bases for XENON1T are fabricated using the same base design. The essential part of

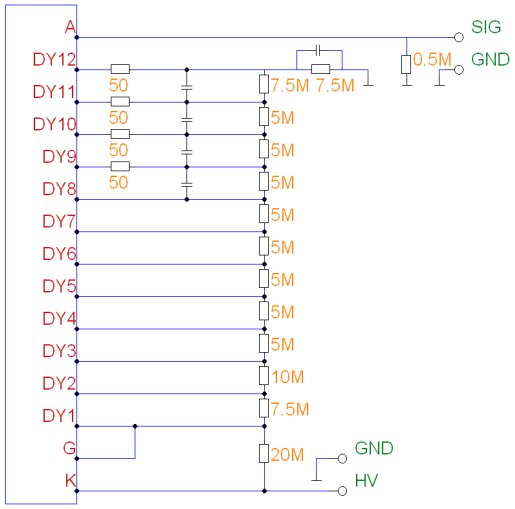

Figure 2.3: *Design of the base [41] used for testing the PMTs at MPIK. The optimal resistance ratios, given by Hamamatsu, were used for this design. The capacitors have capacity values of* 10 nF.

the voltage divider circuit are the 13 resistors, which are connected in series. By means of those, the supply voltage of for example $U = 1500\,\mathrm{V}$, is divided into 13 smaller voltages U_i, which are proportional to the particular restistance R_i (see Equation 1.6) and which add up to U. Fig. 2.3 reveals that not all resistances have the same values. Those near the cathode have higher values to reach the highest possible first multiplication of photoelectrons, which improves the single-photoelectron resolution and the peak to valley ratio of a PMT [42] (these quantities will be introduced in Chapter 3). In Section 1.3 it was pointed out that the linearity of a PMT can be affected by space charges. The latter can occur at dynode stages near the anode, where the electron densities are very high due to the previous multiplication steps. To solve this problem, the resistor values near the anode are also chosen higher than the average, to compensate the electric field resulting from an electron cloud. The capacitors are also included into the voltage divider circuit to improve the pulse linearity [34]. The bases that were built at MPIK can be seen in Fig. 2.4. On the left side, the bottom view shows most

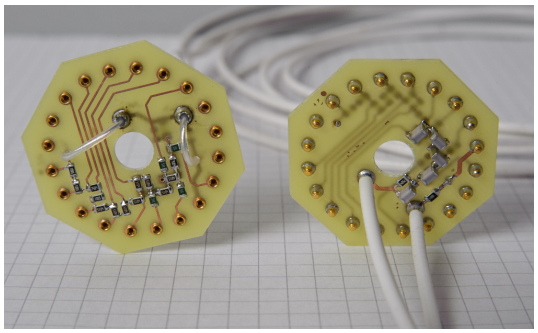

Figure 2.4: *Photograph of the base that was used for testing the PMTs at MPIK [43].*

of the resistors (black) from Fig. 2.3 and the holes to plug in the electrical connectors of the PMT. On the right side the top view on the base shows the five capacitors (gray) and further resistors. The anode output signal of a R11410 PMT in connection with the presented base is shown in Fig. 2.5.

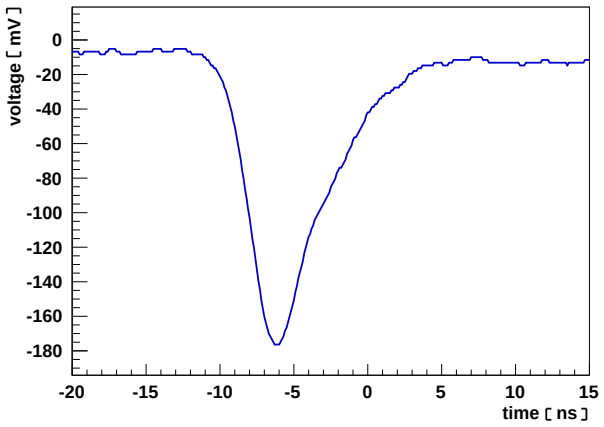

Figure 2.5: *Voltage over time for a typical PMT output pulse after tenfold amplification. This signal has been recorded at an LED illumination of 6 PE. The FWHM of this pulse is* ≈ 5 ns*, the rise time is* ≈ 3 ns *and the fall time is* ≈ 7 ns.

2.2 Testing facilities at MPIK

When testing PMTs, one has to make a compromise between coming as close as possible to the actual conditions of the experiment on the one hand and feasibility on the other hand, since for XENON1T 248 photomultiplier tubes have to be tested. This is done at MPIK in two ways: each PMT is operated at room temperature which is the least time-consuming procedure to confirm if all photosensors work properly after delivery. As a next step, the PMTs are cooled down to around $-100\,°\mathrm{C}$, are tested at this temperature and warm up again. Three of those cooling cycles serve as a thermal stress test. One can classify the PMT measurements in two categories: dark count rate measurements and light-response tests. Therefore, one needs light tight setups with an optional light source, in addition to a high voltage supply and signal readout electronics.

The setup for room temperature measurements is a light tight room, surrounded by metal walls like a Faraday cage, shielding the inside from electromagnetic fields (for further information see [44]). There are twelve PMT slots, each equipped with a light guide providing the PMTs with LED light. The used LED emits UV light with a wavelength of 380 nm. This is larger than the wavelength of LXe scintillation light, 178 nm, but this should not be a problem, because the quantum efficiency of the PMTs is sufficiently large at 380 nm (see [37]) and the performed measurements, described in chapter 3, should not depend on the wavelength of the incoming light. Pulses can be generated with a frequency of 1028 Hz, which means one pulse every millisecond. The LED timing resolution is about 3.3 ns [45], which is smaller than the PMT pulse width of about 5 ns (see Fig. 2.5), but of the same order of magnitude.

A schematic drawing of the used electronics is shown in Fig. 2.6. In addition to the high voltage supply and LEDs, the setup includes readout electronics for several purposes. The first step for the PMT signal for all applications is charge amplification by a factor of ten.

For dark count rate measurements, where PMT pulses have to be counted, the signal is amplified by another factor of ten and afterwards transferred to a discriminator, which sends a logical signal to the scaler if the incoming signal exceeds a certain threshold. Fig. 2.5 shows that the PMT output has a constant noise level unequal to zero. Thus, the discriminator threshold must be set to a level that the noise cannot exceed, but only real pulses can. The

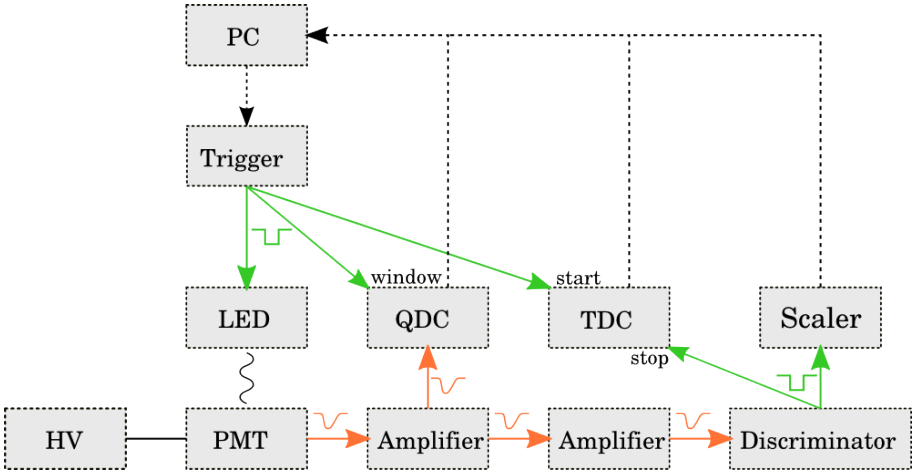

Figure 2.6: *Schematic drawing of the used electronics. A PC manages the trigger, which controls the LEDs, the charge-to-digital converter (QDC) and the time-to-digital converter (TDC). The PMT signals are amplified once or twice by a factor of ten, to be transferred to the QDC or the discriminator. The latter sends a logical signal to the TDC or the scaler. The QDC, the TDC and the scaler transfer their measured data back to the PC.*

scaler then simply counts the logical signals coming from the discriminator.

For measuring the charge of PMT pulses a charge-to-digital converter (QDC) is used. The trigger ensures the following sequence of events, illustrated in Fig. 2.7. First, a LED pulse

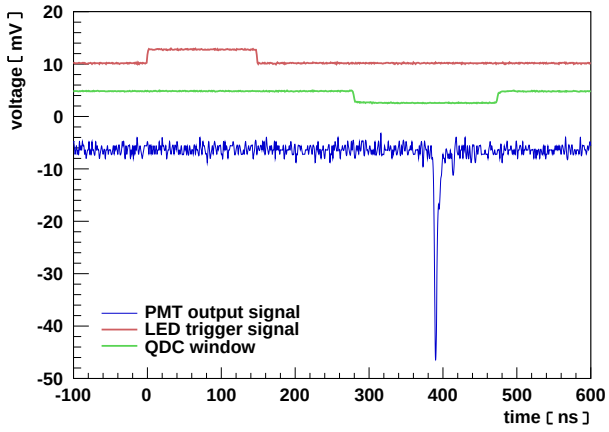

Figure 2.7: *Signals of the PMT, the trigger signal for the LED and the QDC window, viewed on the oscilloscope. The voltage axis is valid only for the PMT signal. The delay between LED trigger signal and PMT pulse is caused by the cables between the trigger and the LED itself.*

is generated, which causes a PMT pulse. After a certain time, when the latter is 10 times amplified and reaches the QDC, the trigger opens the QDC time window for charge integration. The width of this window is set according to the length of a PMT pulse. The QDC resolution is 0.01 pC.

To investigate the timing characteristics of a PMT, a time-to-digital converter (TDC) is used. This device receives a start and a stop signal and converts these into a time difference. For the applications described in this thesis, the start signal is provided by the trigger and the

discriminator sends the stop signal, as can be seen in Fig. 2.6. The TDC resolution is 0.3 ns.

To test the PMTs at LXe temperature, the cooling tank, which is shown opened in Fig. 2.8, is used. Twelve PMTs can be mounted into the two metal structures shown in Fig. 2.9,

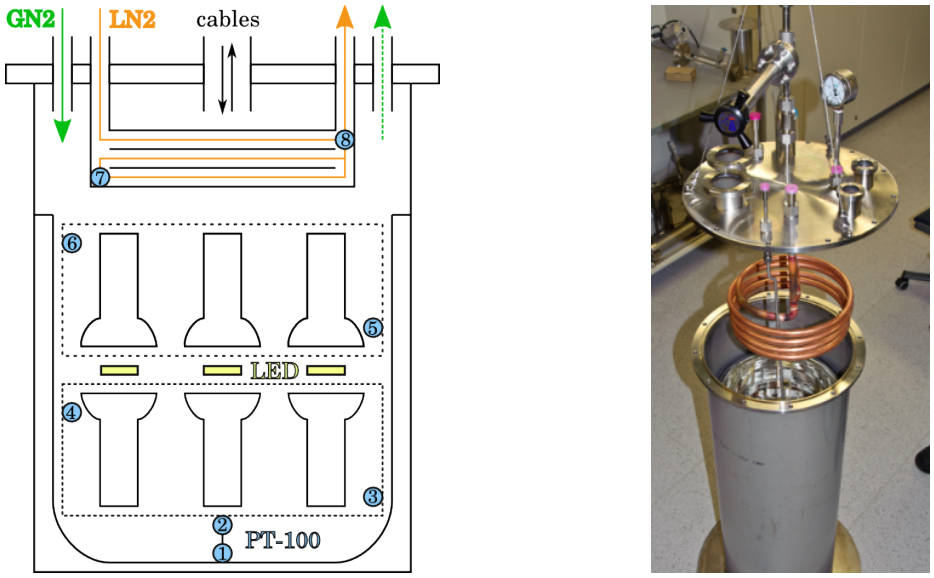

Figure 2.8: *Schematic drawing and photograph of the cooling tank. Eight PT-100 sensors are numbered according to their positions, from the bottom to the top. The yellow LED signs illustrate that the ends of three optical fibers end in this plane, guiding LED light to the PMT windows.*

six in each one, which are then lowered into the dewar inside of the cooling tank. When the latter is closed, the dewar is filled with nitrogen vapor, which is cooled by the liquid nitrogen (LN_2) flow through the copper cooling coil visible in Fig. 2.8. LN_2 cannot be used as cooling medium directly, because it boils at $-196\,°C$ and the desired LXe temperature is only $-100\,°C$. Nitrogen vapor is used instead of air as a medium because the possible condensate, in combination with the electric fields between the PMTs and the holding structure and also between the leads of a PMT, could lead to electric sparks. Of course one could immerse the

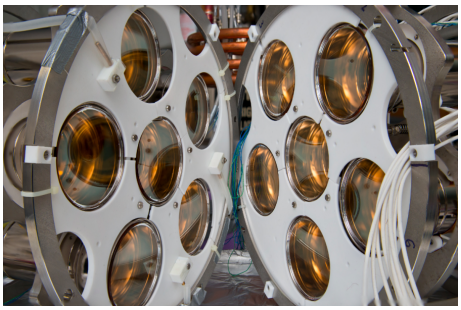

Figure 2.9: *Metal structures holding six PMTs each.*

PMTs into liquid xenon to achieve the right temperature, but this would make the setup much more complex in order not to dissipate or contaminate the xenon too much. The liquid nitrogen flow must be regulated manually while monitoring the temperatures, measured by eight PT-100 sensors, which are placed inside the tank at different heights (see Fig. 2.8). The container is light-tight to enable dark count rate measurements and three optical fibers guide LED light to the plane between the PMTs for light-response tests. On top of the lid, there

are feedthroughs for light guides, high voltage, signal and PT-100 cables, which are connected to the same electronics and LEDs described above.

Fig. 2.10 shows the temperature curves measured by the PT-100 sensors during a typical cool-down. The temperatures T_5 and T_6 are lower than the other two, because the upper sensors are closer to the cooling coil than the lower ones. After four hours, the interior of the whole tank has reached a temperature of around $-100\,°C$. The cooling speed is restricted

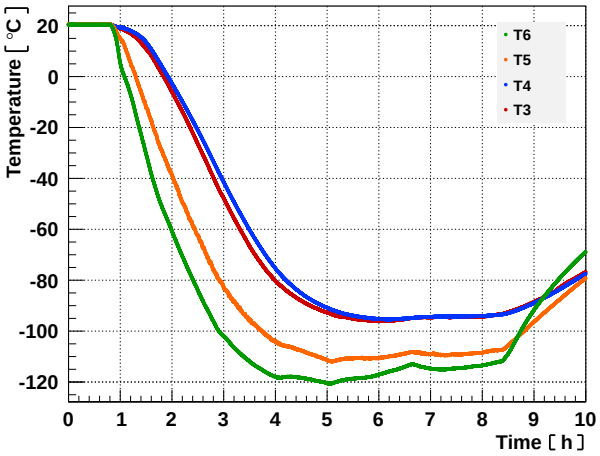

Figure 2.10: *Typical temperature curves of PT-100 sensors during cool-down. The numbers three to five indicate the sensor positions that can be looked up in Fig. 2.8.*

by the manufacturer's indication not to cool the PMTs faster than two Kelvin per minute. During the cold period of several hours, the desired data can be taken. Because permanent LN_2 flow is needed to keep a temperature of around $-100\,°C$, the temperature gradient over the tank is retained during the cold period. Since permanent temperature monitoring and, if necessary, nitrogen flow regulation is needed, the cold period is limited in time. To let the whole tank warm up, the liquid nitrogen flow is stopped. The resulting temperature rise is sufficiently slow due to the good isolation of the tank.

Chapter 3

Photosensor tests and results

This chapter describes the measurements with 91 R11410-21 PMTs and their results, which will be compared to the partially existing manufacturer's specifications. The consequences for XENON1T will be discussed at the end of this chapter.

3.1 Charge spectra

The class of measurements that will be described in this section aims at investigating the charge of PMT pulses under different conditions. The number of electrons contained in the measured electrical PMT pulses is on average the product of the number of photoelectrons that reached the first dynode and the gain of the PMT (see Equation 1.4). The charge Q of an individual pulse is normally distributed around this average, because the electron multiplication by means of the dynode chain is subject to statistical fluctuations. To produce a charge spectrum, the charge values of pulses are recorded over a few minutes and plotted to a histogram. The shape of the resulting depends on several factors: on the one hand on the light intensity and on the other hand on PMT features like gain, charge resolution and peak to valley ratio, which again depend on the operating voltage. Therefore, each measurement is carried out at at constant operating voltage, and constant light intensity of LED pulses. If always the same number of PE was produced in response to a light pulse, the charge spectrum would have a Gaussian shape. But since the number of PE, resulting from a constant light intensity, fluctuates according to Poisson statistics, the resulting charge spectrum has contributions from events with different numbers of PE, all smeared according to Gaussian statistics as mentioned before. The probability that after a light pulse with a certain intensity, k photons are detected, i.e. converted to a photoelectron, is

$$p_\mu(k) = \frac{\mu^k}{k!} \cdot \mathrm{e}^{-\mu}, \tag{3.1}$$

where μ is the mean number of photons detected per light pulse at this particular intensity. A charge spectrum with mainly 1 PE pulses is called single photoelectron or SPE spectrum. It plays a special role because it is used for example to extract the gain of a PMT as it will be shown later. For the purpose of recording an SPE spectrum, the light intensity is set so that during ten LED pulses only one PMT pulse is generated, which corresponds to a Poisson distribution with $\mu = 0.1$. One can calculate from Equation 3.1 that of a certain number of LED pulses, 9.4 % result in a 1 PE pulse, but only 0.5 % in a 2 PE pulse and so on.

A typical measured SPE spectrum is shown by the black histogram in Fig. 3.1. The QDC integration, which has been described in Chapter 2, is carried out after every LED pulse,

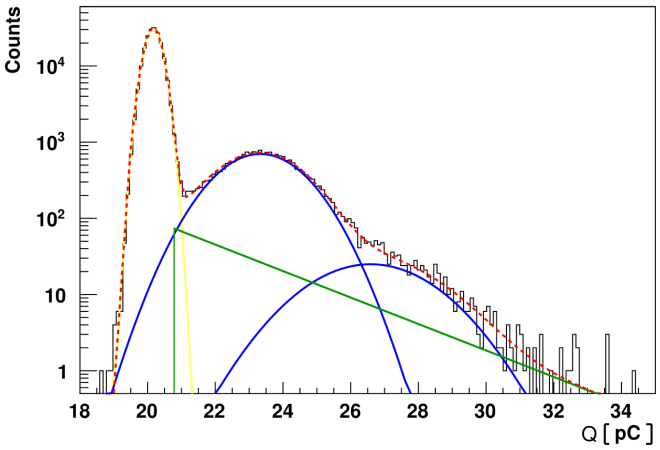

Figure 3.1: *A typical SPE spectrum (black). The fit function (red) [42] has contributions from Gaussian functions for the pedestal (yellow) and for* 1 PE *and* 2 PE *peaks (blue) and from an exponential function (green).*

if there is a PMT pulse or not. In the latter case the baseline voltage is integrated, which results in the left peak, the so-called pedestal. The baseline fluctuates around a non-zero value, because of an offset, which is added to the signal by the electronics. The just mentioned charge offset can simply be subtracted from the signal. Next to the pedestal Fig. 3.1 shows a large Gaussian peak containing 1 PE pulses (middle) and a small 2 PE peak (right). To evaluate a charge spectrum, the shown fit function (red curve) was applied to the data. It has different contributions. The yellow curve is a Gaussian function (f_0) fitted to the pedestal, the blue curves are Gaussian functions fitted to 1 PE (f_1) and 2 PE (f_2) peaks, where

$$f_i(Q) = c_i \cdot \exp\left\{-\frac{(Q-\mu_i)^2}{2{\sigma_i}^2}\right\} \quad \text{for } i \in \{1,2,3,4\} \tag{3.2}$$

and contributions up to 4 PE can be accounted for, which is necessary for higher light intensities. The green curve is an exponential function, which was introduced to empirically improve the overall fit. The gain g of a PMT can be extracted from a SPE spectrum as

$$g = \frac{\mu_1 - \mu_0}{10 \cdot e}, \tag{3.3}$$

where e is the elementary charge and the factor 10 takes into account the amplification between PMT and QDC (see Fig. 2.6). The width σ_1 of the SPE peak is used to calculate the SPE resolution:

$$R = \frac{\sigma_1}{g}\,. \tag{3.4}$$

Not only the resolution is an important quantity to characterize how well signal and noise can be separated, but also the peak to valley ratio P/V. It is obtained when the maximum of the 1 PE peak P is divided by V, which is the minimum of the valley between noise and 1 PE peak.

The dependency of a charge spectrum on the light intensity is illustrated in Fig. 3.2. The charge axis is converted from Coulomb to PE in the following way:

$$Q\,[\mathrm{PE}] = \frac{Q\,[\mathrm{C}] - \mu_0\,[\mathrm{C}]}{10 \cdot e \cdot g}\,. \tag{3.5}$$

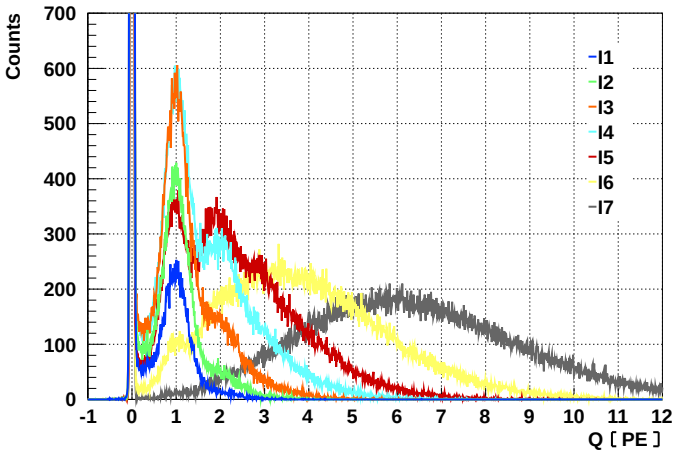

Figure 3.2: *Charge Spectra at different LED light intensities I1 < I2 < ... < I7, at an operating voltage of* 1500 V *for all measurements.*

Equation 3.3 emerges from Equation 3.5 when setting $Q\,[\mathrm{PE}] = 1$. One can see in Fig. 3.2 that the position of the pedestal is not affected by the light intensity as it is expected. The lowest intensity results in a SPE spectrum, whereas at medium intensities contributions from 1 PE as well as from 2 PE and 3 PE are visible separately. The relative amplitude of each peak obeys Poisson statistics. The absolute integral over the spectrum, apart from the pedestal, increases for increasing LED intensity up to a certain point, because for higher illumination a 0 PE event gets more and more unlikely. To have a baseline integration also for high intensities, every second LED pulse is skipped, while the QDC integration takes place anyway. For the highest intensity the single contributions add up to form a wide featureless peak.

The dependency of a SPE spectrum on the operating voltage value is illustrated in Fig. 3.3. One can see that the pedestal stays at the same position again. The single photoelectron peak

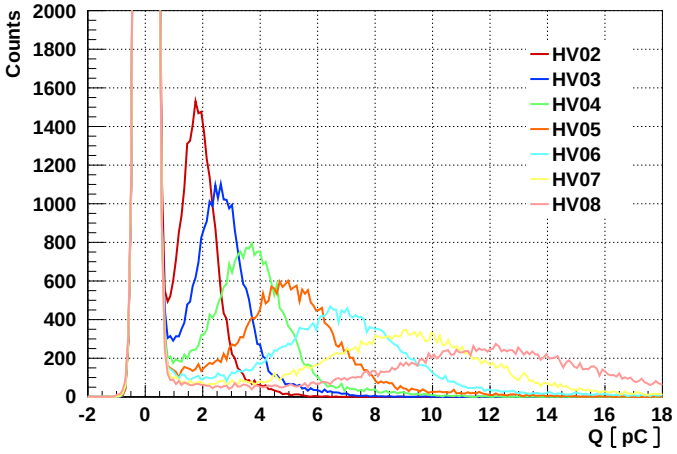

Figure 3.3: *SPE spectra at different operating voltages. The charge offset μ_0 was subtracted. The voltage abbreviations are defined in Table A.1.*

on the other hand becomes wider and is shifted to higher charge values for higher voltages.

In the following, the dependency of the PMT features gain, SPE resolution and $^{P}/_{V}$ on the applied operating voltage are discussed. For this purpose the SPE spectra from 91 PMTs, recorded at eight different voltages each, were used. In XENON1T all PMTs will be operated at the same gain and not at the same operating voltage. This avoids the need for a correction of PMT signals, which would add another uncertainty to for example the vertex position reconstruction from the $S2$ signal pattern on the PMTs. Thus, it is desirable to investigate the dependency of the peak to valley ratio and resolution not only on operating voltage but also on gain, which will also be done in the following sections.

3.1.1 Gain

A histogram of gain values for an operating voltage of 1500 V, using the data of all 91 PMTs, can be seen in Fig. 3.4. In the first data sheet of the R11410-21 PMT, Hamamatsu originally

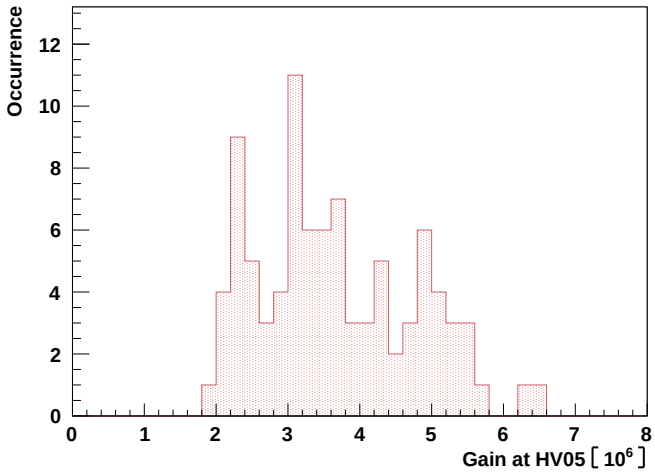

Figure 3.4: *Gain values of 91 PMTs at an operating voltage of* 1500 V.

specified a typical gain of $5 \cdot 10^6$ at this voltage. But Fig. 3.4 shows that most gain values are smaller than the specification. The mean value is $3.7 \cdot 10^6$ and the standard deviation $1.1 \cdot 10^6$.

The dependency of the gain on the operating voltage is illustrated in Fig. 3.5. The fact that the gain increases with increasing operating voltage confirms the observation from Fig. 3.3, that the SPE peak is shifted to the right for higher voltages. For one voltage the gain values of different PMTs are different because of statistical fluctuations in the manufacturing process. From Equation 1.7 one can deduce

$$g(U) = \tilde{g} \cdot \left(\frac{U}{\tilde{U}}\right)^{k \cdot n}, \tag{3.6}$$

where $n = 12$ is the number of dynodes, k is an unknown photocathode material-specific parameter and $\tilde{U}$ is the operating voltage, which corresponds to a gain of $\tilde{g}$. In Fig. 3.5, the gain values of two single PMTs are colored orange and green, respectively. The curves through the data points are fit functions according to Equation 3.6 with the parameters n and $\tilde{g}$ fixed. The parameter k, which is determined by the dynode structure and material typically has a value between 0.7 and 0.8 [34]. Our fit result for k is 0.65 for both PMTs, which does not

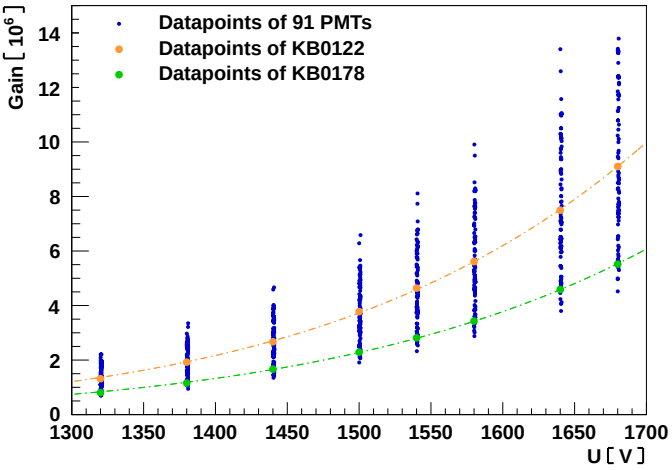

Figure 3.5: *Gain values of 91 PMTs at eight different operating voltage values each. The dashed curves are fit functions according to Equation 3.6.*

exactly agree with the literature values, but has the same order of magnitude. The value $\tilde{g}_0 = 3 \cdot 10^6$ was chosen as reference gain and the corresponding operating voltage $\tilde{U}_0$ results from the fit. Note that the values for $\tilde{U}_0$ are in general not equal for different PMTs. For the PMT KB0122 for example $\tilde{U}_0 = 1460$ is obtained. We have defined $\tilde{U}_1$ as the voltage corresponding to a gain of $\tilde{g}_1 = 2 \cdot 10^6$, which was the operating gain in XENON100. The question which gain value is the best solution for XENON1T will also be addressed in the following.

3.1.2 Peak to valley ratio

The dependancy of the peak to valley ratio on the applied voltage is illustrated in Fig. 3.6 (left). Each blue dot results from a measurement of one SPE spectrum of one PMT at one of

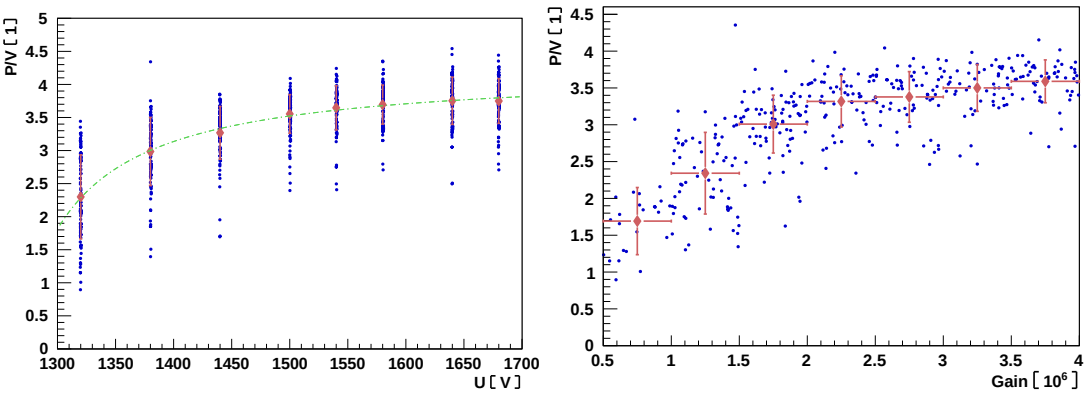

Figure 3.6: *Peak to valley ratios of 91 PMTs at eight different operating voltage values each (blue dots). Left: The red dots and error bars are mean and standard deviation values calculated for each voltage. The fit function (green)* $P/V(U) = \frac{-c_0}{c_1(U-c_2)} + c_3$ *has no physical meaning. Right: Peak to valley ratios versus the gain of each PMT. The red dots and vertical error bars are mean and standard deviation values calculated for slices with a width of* $0.5 \cdot 10^6$ *as it is illustrated by the horizontal bars.*

eight different operating voltage values. This plot shows that higher voltages result in higher and thus better $^{P}/_{V}$ values. The spread at one voltage is very large, because all the PMTs have different gain values and the peak to valley ratio depends on the gain of the PMT. Therefore, in Fig. 3.6 the dependency on the gain value is also shown. Again, one blue dot corresponds to one PMT operated at one of the eight voltages. For low gain values, the SPE peak is located very close to the pedestal, which enhances the valley and thus results in a low peak to valley ratio. It improves for higher gain values, because the SPE peak is separated further from the pedestal. Because this effect is stronger for small gain values, the curve flattens around a gain value of $2 \cdot 10^6$. The indication from the data sheet that the peak to valley ratio at 1500 V operating voltage is at least 2.0 can be confirmed.

3.1.3 Single photoelectron resolution

The dependency of the single photoelectron resolution on the applied voltage and on the gain is illustrated in Fig. 3.7. Higher voltages result in larger gain values, which again leads to

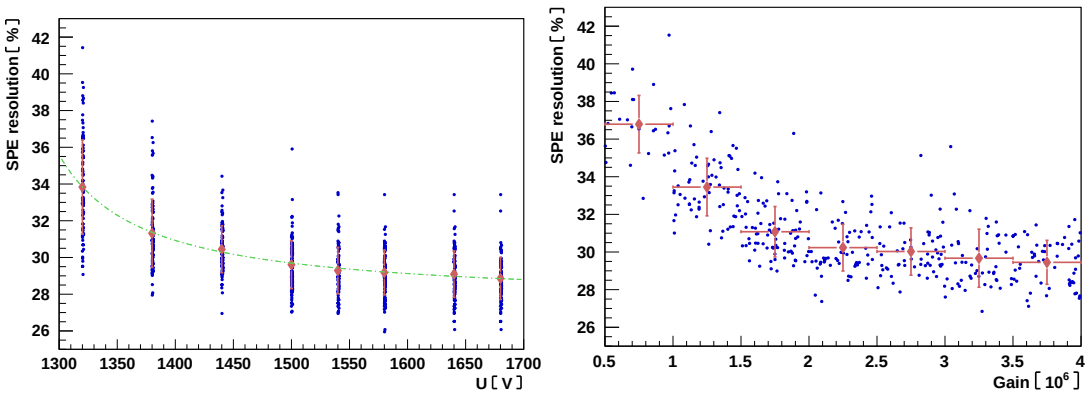

Figure 3.7: *Left: SPE resolution of 91 PMTs at eight different operating voltages. The red dots and error bars are mean and standard deviation values calculated for each voltage. The fit function* $R(U) = \frac{+c_0}{c_1(U-c_2)} + c_3$ *has no physical meaning. Right: SPE resolution versus the gain of each PMT. The red dots and vertical error bars are mean and standard deviation values calculated for slices with a width of* $0.5 \cdot 10^6$ *as it is illustrated by the horizontal bars.*

lower and thus better resolution values.

One can combine the results for the SPE resolution and the peak to valley ratio to get the ideal operating gain value for XENON1T. The lowest possible R and the largest possible $^{P}/_{V}$ is desired at the lowest possible operating voltage, because the heat dissipation increases with increasing voltage. From Fig. 3.6 and Fig. 3.7 one can see that the curves, describing the dependency of the resolution and the peak to valley ratio on the gain, both become much more flat for gain values larger than $2 \cdot 10^6$. While changing the gain from $1 \cdot 10^6$ to $2 \cdot 10^6$ increases the peak to valley ratio by 63 % and decreases the resolution by 13 %, shifting the gain further from $2 \cdot 10^6$ to $3 \cdot 10^6$ increases the peak to valley ratio only by further 6 % and decreases the resolution only by further 2 %. Therefore, a gain of $2 \cdot 10^6$ should be a good compromise. Fig. 3.8 shows that the operating voltages, which correspond to this gain have values between 1290 V and 1520 V and a mean value of $\tilde{U}_1 = (1400 \pm 50)$ V.

The measurements described in this section were carried out in the room temperature setup, but the consistency with measurements at liquid xenon temperature has been checked. We found that the same optimal gain value is deduced from the measurements at −100 °C.

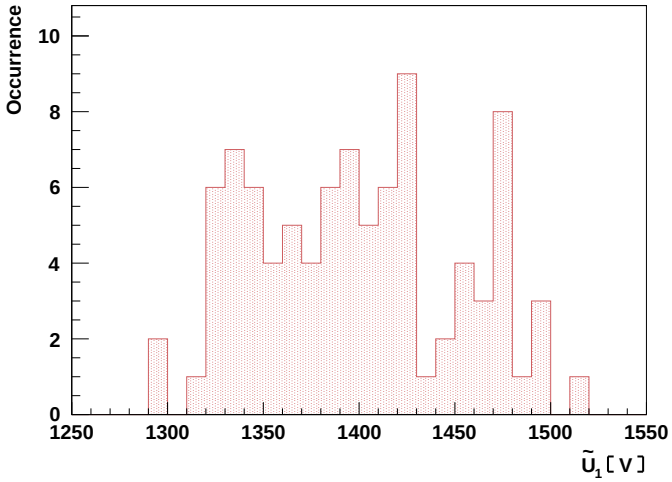

Figure 3.8: *Needed operating voltage to receive a gain of* $2 \cdot 10^6$*. It was calculated for each of 91 PMTs using Equation 3.6.*

3.2 Dark count rate at room- and liquid xenon temperature

As described in Section 2.2, the dark count rate is measured while the PMTs are not exposed to light. A scaler counts pulses that exceed the discriminator threshold, which ensures on one hand that upward fluctuations of the baseline are not counted as PMT pulses and on the other hand that all real pulses are detected. The threshold was set once to 25 % of the signal amplitude for all channels, when all PMTs were operated at $U = \tilde{U}_0$, i.e. had a gain of $3 \cdot 10^6$. Given the linearity of both the signal amplitude and the signal integral i.e. the charge, this threshold corresponds to a charge of 0.25 PE. Due to this threshold, the dark count rate depends on the gain of the mounted PMT and thus also on the applied voltage. For a PMT with a larger gain value more pulses exceed the same threshold, which can be understood by looking at Fig. 3.3: If the threshold was set to 0.25 PE with reference to the orange curve, most of the pulses are counted for this PMT. But if another PMT has a gain like the red curve illustrates, almost half of the pulses cannot exceed the threshold. This is why all dark count rate comparing measurements should be carried out at $\tilde{U}_0$ voltage. The scaler counts pulses over a time interval of one minute. Afterwards this value is divided by 60 to get the rate in Hz.

For every PMT first of all the dark count rate at room temperature is checked. According to Hamamatsu specifications, its value is around 4000 Hz but should not be larger than 10 000 Hz when setting an appropriate threshold. A typical measurement is shown in Fig. 3.9. The rate is plotted over time for 12 PMTs mounted in the room temperature setup described above. The plot shows that the dark count rates decrease for a few hours before they reach their final value. This is because when the PMTs are mounted into the Faraday room, they are exposed to ambient light for a short time, which can excite the atoms in the PMT materials e.g. the window. The subsequent de-excitation produces photons, which could be responsible for the enhanced rates. The rate of PMT KB0128 does not exceed 10 000 Hz, but it fluctuates strongly over the whole measurement time whereas the other rates are stable. Electronic noise as a cause of such fluctuations can be excluded by viewing the signal on the oscilloscope and

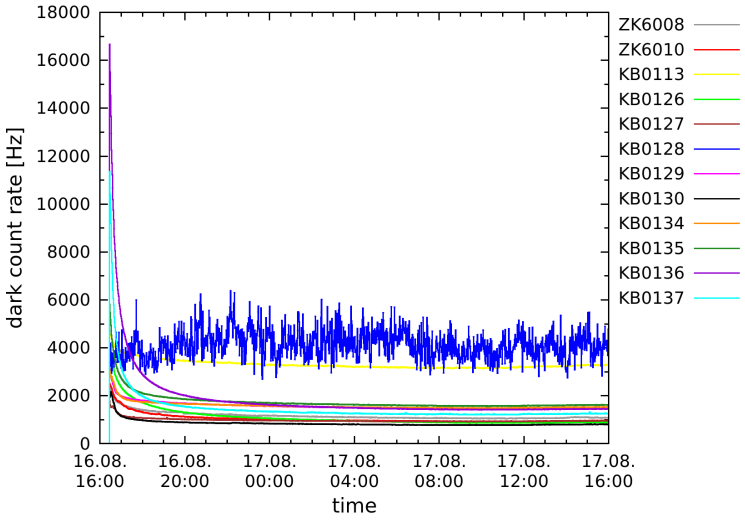

Figure 3.9: *Typical dark count rate measurement in room temperature setup.*

observing normal pulses. After this measurement, the PMT KB0128 will not be employed for XENON1T and was replaced by Hamamatsu. A histogram of room temperature dark count rates is shown in Fig. 3.10. Very unstable rates like the one of KB0128 in Fig. 3.9, which

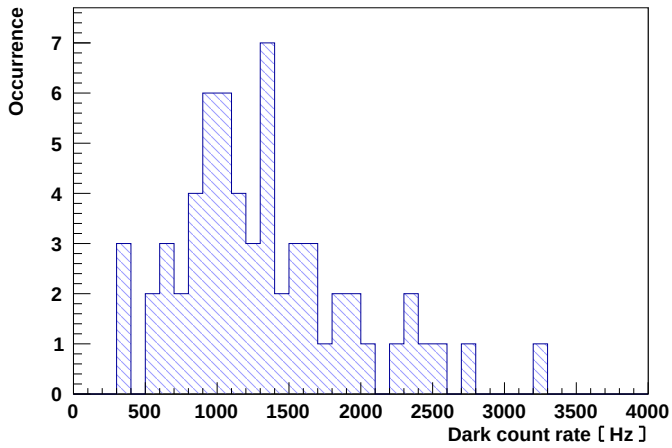

Figure 3.10: *Histogram of dark count rates at room temperature and* $U = \tilde{U}_0$*. The mean value and the standard deviation of the available data of 62 PMTs is* 1290 ± 560 *Hz.*

varies by more than 1000 Hz, are not included in this histogram. It shows that all rates are even lower than the typical value of 4000 Hz.

How the dark count rate evolves with decreasing temperature is illustrated in Fig. 3.11. To create this plot, the dark count rates of three PMTs in the upper support structure were used. Because the temperature of the photocathode is relevant for the dark count rate, the temperature of PT-100 sensor number 5, which is the closest one to the upper PMT windows, was correlated with the rates. The dark count rate of a PMT at one specific photocathode temperature should be the same, independent on the fact if the PMT is cooled down or warms up. Looking at the green curve in Fig. 3.11 this seems not to be the case. Therefore,

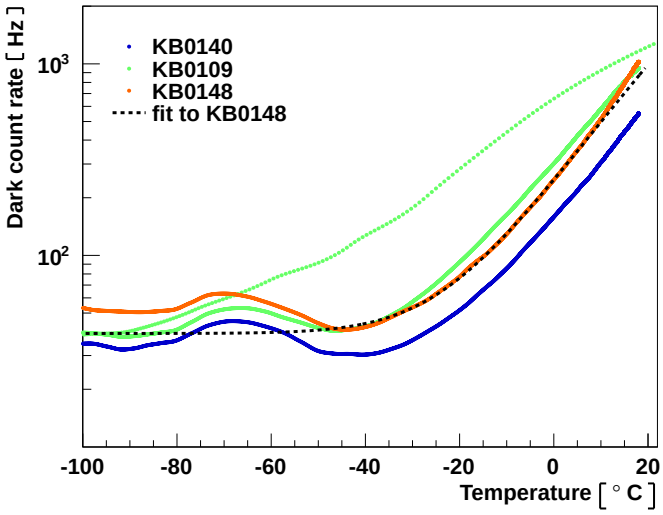

Figure 3.11: *Dark count rate dependency on the temperature. The green dotted curve shows the data of PMT KB0109 during cooling down the PMTs and the solid lines illustrate how the dark count rate evolves while letting the whole system warming up. The black dashed curve is a fit to the rate of KB0148 according to Equation 3.7.*

it is probable that the measured temperature does not describe the actual photocathode temperature in both cases due to limited heat conduction. Since during warming up the temperature changes very slowly, the situation in the cooling tank should be close to a thermal equilibrium. Therefore, the solid lines should describe the actual dependency of the dark count rate on the temperature better than the dashed line. Fig. 3.11 shows that the dark count rates at $\approx -40\,°\mathrm{C}$ have the similar low values as those at $-100\,°\mathrm{C}$. This implies that the thermionic emission does not play a role anymore below $\approx -40\,°\mathrm{C}$ and the other dark count rate components become more important. The rise of dark count rates between $-100\,°\mathrm{C}$ and $\approx -40\,°\mathrm{C}$ is probably not a real temperature effect, because according to Equation 3.7, a curve which is monotonously decreasing with decreasing temperature is expected. A possible explanation can be given by different expansion coefficients of the PMT materials. Due to the sudden rise of temperature after operation at a constant temperature for several hours, the geometry inside of the PMT could slightly change, resulting for example in an enhanced collection efficiency for a certain time, which could explain the increased dark count rate. The fit function shown in Fig. 3.11

$$DC(T) = A \cdot T^{5/4} \cdot \mathrm{e}^{-B/T} + C \tag{3.7}$$

is the sum of two dark count rate components. The first term is the temperature-dependent part according to Equation 1.8 with $B = {}^{W}/_{k_B}$, which is due to thermionic emission of electrons from the photocathode. The second term C is due to cosmic ray particles or radioactivity and independent of the temperature. The fit is quite good over a range of 50 K during the warm-up process. From the fit result for the parameter $B\,[\mathrm{K}]$ an estimate for the work function of the bialkali photocathode can be given. The result $W = 0.5\,\mathrm{eV}$ is a plausible value, even if it is only a rough estimate. The work functions of alkali metals have values around 1 to 2 eV, but the work function of the special bialkali material should be lower to allow for such an exceptionally high quantum efficiency.

The specifications state that the value for the dark count rate at −100 °C is typically around 50 Hz but should not be larger than 200 Hz. Another requirement is a stable rate, which is even more important at the XENON1T operating temperature, −100 °C, than at room temperature. For about 15 % of the PMTs this was not the case and one or both of two anomalous behaviors was observed, which can both be explained by light production of the PMT itself. The first abnormal behavior is a sudden rise and a subsequent slow decline of the dark count rates of two opposite PMTs as it is shown in Fig. 3.12. Opposite means that the entrance windows face each other (see Fig. 2.8). This effect can be explained by a sudden light

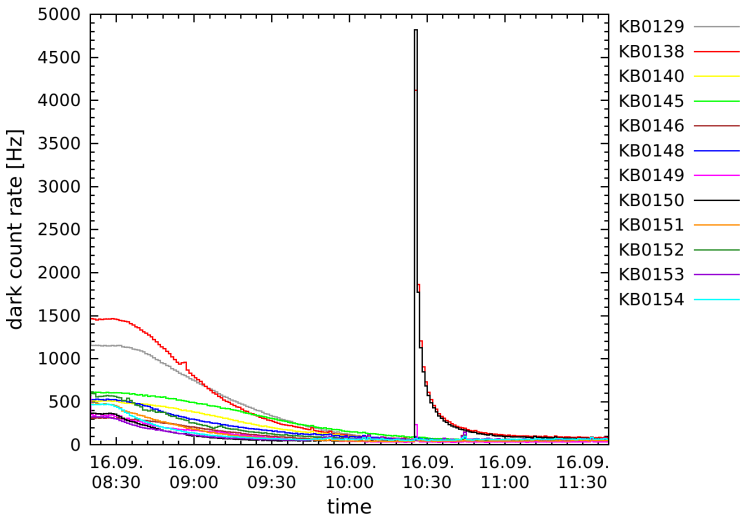

Figure 3.12: *Dark count rate measurement during a cool-down with operating voltages of* $U = 1500\,\mathrm{V}$. *After the rates decreased due to their temperature dependency, those of two opposite PMTs, KB0138 and KB0150 suddenly rise and afterwards slowly decrease.*

flash in one of these two PMTs. This light would be seen clearly only by the affected PMT and the opposite one, because the two PMT support structures are only about 1 cm away from each other. A light flash with many photons can result in the same excitations and light producing de-excitations that also ambient light causes (see Fig. 3.9). This can explain the fact that the rates do not return to their previous low values immediately. After sending some of the affected PMTs back to Hamamatsu, they found that electric sparks occur between the dynode connecting metal rods (see Fig. 2.2), because space charges build up on the ceramic stem.

The second anomaly is the continuous correlation of unstable or increased dark count rates of two opposite PMTs as it can be seen in Fig. 3.13. This effect can be explained by the constant light emission of one PMT at a low intensity, which is again only seen by itself and the opposite PMT. The correlation is checked by switching one PMT off. When no voltage is applied to the problematic PMT, the sparking stops and the rate of the opposite PMT returns to it's normal value. A dependency of the intensity or occurrence of the latter effect on the operating voltage has been observed. The same procedure as in Fig. 3.13 has been performed while operating the PMTs at a lower voltage of 1500 V. In this case it was found that while PMT KB0137 is switched on, the rate of the opposite PMT KB0156 is compatible within errors with the rate when PMT KB0137 is switched off. The operating voltage dependency of the effect can be explained by the fact that electric sparks between the metal rods are more probable for higher potential differences between them, which is the case for a higher operating voltage.

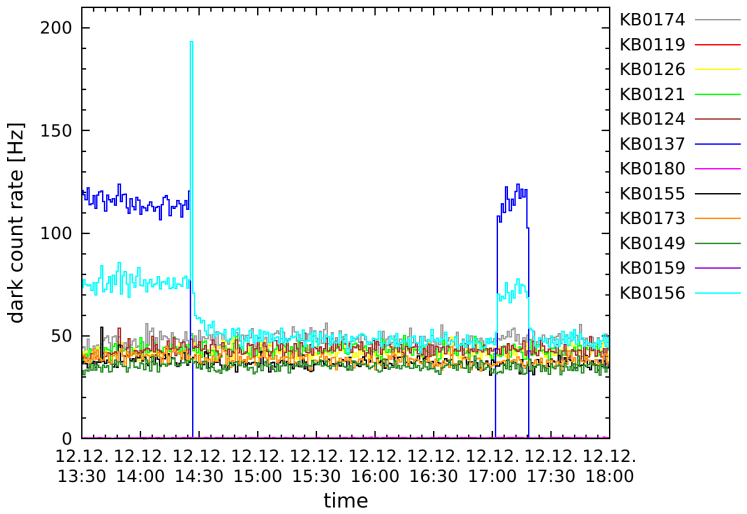

Figure 3.13: *Dark count rate measurement during the cold period of a cool-down ($U = 1600\,\mathrm{V}$). While PMT KB0137 is switched on, the rate of the opposite PMT KB0156 is enhanced. When PMT KB0137 is switched off at ≈14:30 h, the rate of PMT KB0156 decreases from (76±4) Hz to (48±2) Hz after a short time. The peak of the rate at this point is an electronic effect. For a few hours all PMTs have dark count rates around* 40 Hz. *Switching PMT KB0137 on again at ≈17:00 h enhances the rate of PMT KB0156 again.*

Light production is a clear indication for not using the concerning PMT in XENON1T. Therefore, 5 PMTs have been replaced by Hamamatsu and other problematic ones are still under investigation. The company has been working on a solution, which includes rearranging the dynode connections to reduce the potential differences between pairs of rods. The new design will be realized for the next batches of PMTs.

A histogram of dark count rates measured during the cold period of a cool-down is shown in Fig. 3.14. It reveals that most values accumulate around 40 Hz, which is close to the typical value of 50 Hz given by Hamamatsu. Higher dark count rates indicate that this or the opposite PMT might have emitted light (compare Fig. 3.13).

In XENON1T one condition for a valid $S1$ signal is the simultaneous detection of two PMT signal s within a certain coincidence window. A low dark count rate is important because the probability for an accidental coincidence due to two dark counts within this window should be as small as possible to keep the background low.

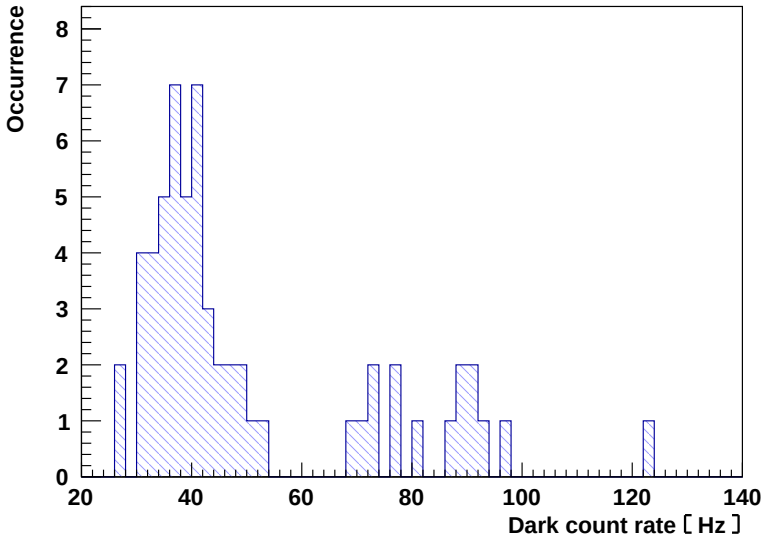

Figure 3.14: *Histogram of dark count rates at LXe temperature of 60 PMTs operated at* $U = \tilde{U}_0$.

3.3 Time characteristics

The basic time characteristics of a R11410 PMT pulse were already shown in Fig. 2.5. The pulse shape is mainly determined by the design of the voltage divider circuit. The width of the R11410 pulse is of the order of nanoseconds. It depends, as well as the rise- and fall time, on the amount of charge that flows through the anode and thus on the gain of the PMT and on the external conditions like light intensity and applied voltage.

3.3.1 Transit time

The feature characterizing the time response of a PMT is the so-called transit time (TT). It is defined as the time difference between the emission of a photoelectron at the photocathode and the point in time when the multiplied electron pulse reaches the anode. The TT can be determined by measuring the time that passes between the emission of a light pulse and the maximum of the following PMT pulse, as it is illustrated in Fig. 3.15. The time that the light

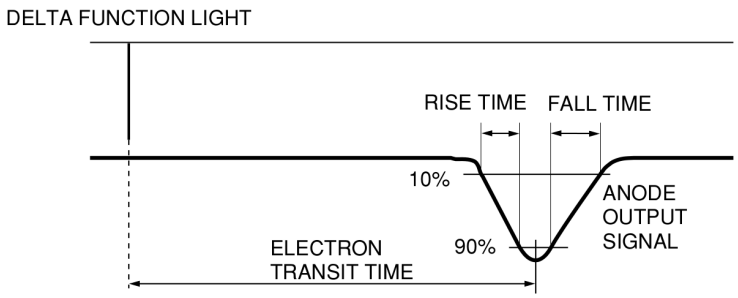

Figure 3.15: *Definition of the electron transit time [34].*

needs to reach the photocathode can usually be neglected compared to the electron transit time.

The important feature for the time resolution of an experiment, also for XENON1T, is

the spread of transit times (TTS). Depending on the point where a photon hit a PMT photocathode, and on the momentum direction of the emitted photoelectron, the paths to the first dynode are not of equal length and also the electron might be exposed to slightly different electric field strengths on its way. These factors can affect the transit time [46]. Thus, when exposing several PMTs to light simultaneously, the times of the generated PMT pulses can vary. Therefore, the transit time spread defines amongst others how short the coincidence window can be chosen in XENON1T.

By means of the MPIK setup, the TT is measured using the LED as light source, which illuminates the whole PMT window. The measurement technique is the following. The TDC, which was introduced in Chapter 2, receives a start signal by the trigger, which simultaneously triggers the LED. The stop signal is provided by the discriminator when the PMT pulse exceeds the discriminator threshold. The measured time is not the absolute TT for two reasons. Firstly, the measured time difference includes the propagation times through the cables and electronics. The second reason is that the TT measurement does not stop at the maximum of the pulse but at the beginning when the signal exceeds the discriminator threshold of 0.25 PE (related to a pulse containing $3 \cdot 10^6$ electrons). Due to the short rise time of ≈ 3 ns, the latter effect is small compared to the effect of the cables. Since the just described time offset is the same for all pulses, by means of this method the transit time *spread* can be measured exactly.

A histogram of transit times is shown in Fig. 3.16. The large peak contains the regularly

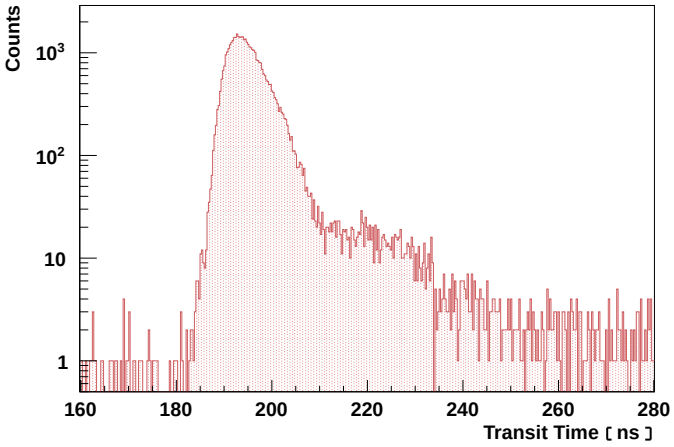

Figure 3.16: *Histogram of transit times plus offset of the PMT KB0113.*

multiplied pulses whereas the excess of counts right to the main peak is due to late pulses, which appear when a photoelectron is backscattered at the first dynode (see Section 1.3). The measured transit time from Fig. 3.16 is 195 ns on average. Since the actual transit time is typically 45 ns for this PMT model according to Hamamatsu, the aforementioned time offset has a value of ≈ 150 ns. The full width at half maximum (FWHM) of the large peak containing the normal pulses is defined as transit time spread.

The measurement that is shown in Fig. 3.16, as well as all other TTS measurements were carried out at SPE light intensity, because more than one photoelectron at a time would misleadingly reduce the transit time spread. A larger intensity enhances the pulse width and an excess of the discriminator threshold can therefore be achieved earlier. The TTS slightly depends on the gain of a PMT for the same reason: a larger pulse can exceed the threshold earlier. Therefore, the operating voltage $\tilde{U}_0$ was used to have the same gain for all PMTs.

Hamamatsu specified that the transit time spread of the R11410 PMT is typically 9 ns. According to Fig. 3.17 the mean TTS value of the XENON1T PMTs measured so far is 8.7 ns. Note that an LED pulse is not a delta function light as Fig. 3.15 suggests. It has a

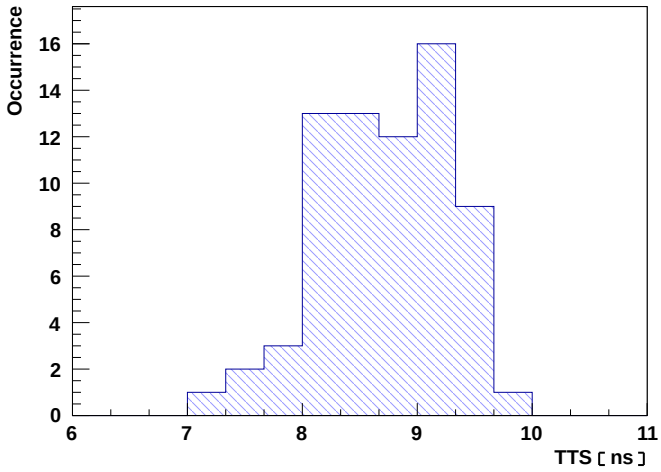

Figure 3.17: *Histogram of TTS values measured at SPE intensity and $\tilde{U}_0$ voltage. The mean value $\pm$ the standard deviation of the available data of 70 PMTs is* 8.7 ± 0.5 *ns.*

finite resolution, which adds an additional spread to the transit times. If one assumes that the instant of time of the LED pulse as well as the time of the PMT pulse are normally distributed, the corrected transit time spread can be calculated as

$$TTS_{\mathrm{PMT}} = \sqrt{TTS_{\mathrm{exp}}^2 - FWHM_{\mathrm{LED}}^2}, \tag{3.8}$$

where TTS_{exp} is the measured transit time spread and $FWHM_{\mathrm{LED}} = 3.3$ ns the LED resolution introduced in Section 2.2. It was deduced from measuring the TTS with laser as light source with a resolution of the order of ps, in addition to the measurement with the LED [45]. The corrected result is then $TTS_{\mathrm{PMT}} = 8.0$ ns. Due to the causes for the transit time spread, the PMT pulses are not exactly normally distributed. Plotting the TTS on a logarithmic scale like in Fig. 3.17, one can see the asymmetry of the peak. But for the calculation above the assumption should be justified.

3.3.2 Afterpulses

Afterpulses can look like real, incident photon induced, pulses. Thus, just like dark counts, they can cause accidental coincidences in the XENON1T detector.

Since they are time-correlated with the main pulse, their occurrence is investigated using the TDC of the MPIK setup. Within the TDC time window of 1.2 µs, the first pulse after a main pulse is detected and the time difference is measured. To do so, main pulses are induced by an LED pulse, the trigger also gives a start signal to the TDC. The stop signal is again provided by the discriminator. In contrast to the TTS measurement, where the main pulse is inducing the TDC to stop, in this measurement the first pulse after the main pulse should stop the TDC time window, because this is the afterpulse. To achieve this, the LED and TDC start are not triggered simultaneously, but the TDC start is delayed until the main pulse is over, as the green curve shows in Fig. 3.18. This sequence is repeated half a million times, given

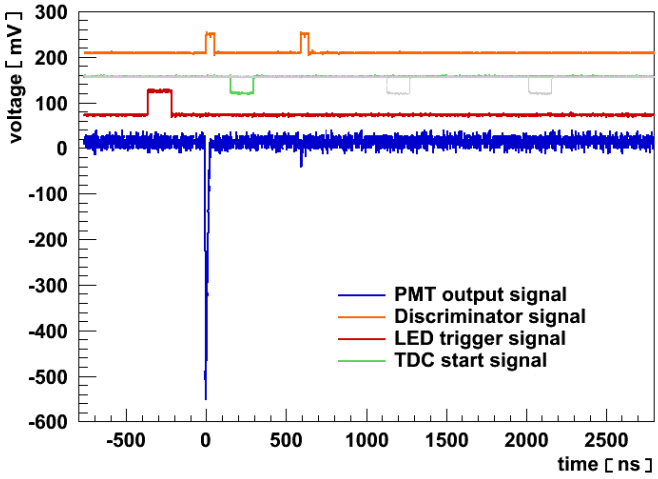

Figure 3.18: *Afterpulse measurement. After the TDC started (green) the discriminator (orange) stops the TDC when an afterpulse is detected. The voltage axis is valid for the PMT signal only. Note that the main pulse is much larger than the afterpulse because of an LED illumination of* $\approx 20\,\mathrm{PE}$. *The gray curve shows the TDC start position of two further measurements.*

a measurement time of $500s$ and the LED pulse frequency of 1028 Hz. To detect afterpulses occurring within 3 µs instead of only 1.2 µs after the main pulse, the same measurement is repeated two times, with an additional delay of 1 µs and 2 µs, respectively (see the gray curves in Fig. 3.18). To get better statistics on how many afterpulses are generated by a certain number of photoelectrons, an LED intensity I_{LED} much higher than SPE is used ($\approx 20PE$). The afterpulse probability, that one PE leads to at least one afterpulse, is then

$$APP\,[\%] = \frac{N_{\mathrm{AP}}}{N_{\mathrm{MP}} \cdot I_{\mathrm{LED}}\,[\mathrm{PE}]}, \tag{3.9}$$

where N_{AP} is the number of measured afterpulses and N_{MP} is the number of main pulses, which is calculated from the overall measurement time and the LED pulse frequency. The LED intensity cannot be set in units of PE but in terms of a number on an unknown scale. Therefore, for every PMT channel, the LED intensity has to be measured. This is accomplished by recording a charge spectrum which looks like the gray curve in Fig. 3.2 and using a fit routine, similar to that from Fig. 3.1, with more Gaussian components [42], and calculating the maximum point of the resulting fit curve to the data to use it as I_{LED}.

Of course there can be more than one afterpulse within a 1.2 µs time window. This is not accounted for when using the measurement technique described above, because the used TDC can only record a single stop signal during its measurement time. Thus, a correction of the measured data is needed. The measured time difference is arranged in bins with a width of 0.3 ns, which was chosen according to the TDC resolution. One assumes that in one bin, during one pulse sequence, either one afterpulse is detected, or none, which implies Poisson statistics. It is obvious that the content of the first bin does not need any correction because no earlier pulse could have prevented the detection of an afterpulse. The probability that there is an event in the second bin is equal to the probability that there was no afterpulse in the time of the first bin. These informations can be used, in combination with the number of main pulses and the measured bin content of the first bin, to correct the content of the second bin. Afterwards, the third bin is corrected, and so on. For more detailed information, see [43].

A typical corrected afterpulse spectrum can be seen in Fig. 3.19, showing which time differences have been measured how many times between main- and afterpulse. Each peak

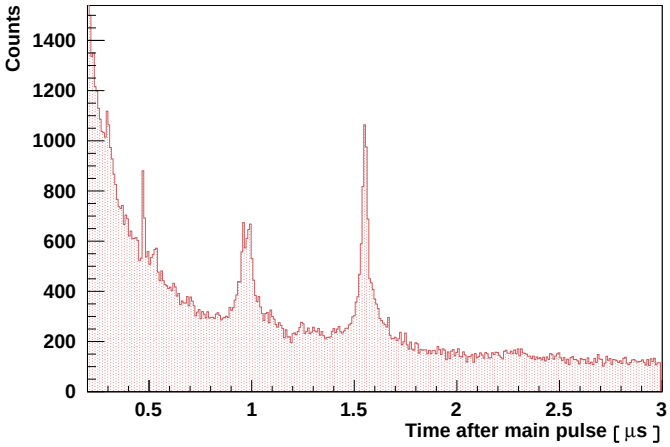

Figure 3.19: *Typical afterpulse spectrum, here of PMT KB0112.*

corresponds to a molecule type in the residual gas inside of the PMT because when a molecule gets ionized by a photoelectron and is accelerated back to the photocathode, the time it needs for that path depends on its mass (also on the voltage applied between the cathode and the first dynode). The resulting delay determines the time between the main- and afterpulse, the so-called afterpulse time. The larger the mass of the ion, the longer the afterpulse time. The afterpulse times found for KB0112 in Fig. 3.19 are at $AT_1 \approx 0.3\,\mu s$, $AT_2 \approx 0.5\,\mu s$, $AT_3 = (0.9 - 1.1)\,\mu s$ and $AT_4 = (1.4 - 1.7)\,\mu s$. Not all of those appeared for all other R11410-21 PMTs but those are the only afterpulse times that were found. Possible components of the residual gas are for example hydrogen (H_2), methane (CH_4), carbon monoxide (CO) and -dioxide (CO_2) [37].

To calculate the afterpulse probability, the number of afterpulses N_{AP} is calculated by integrating over the whole spectrum from 0 µs to 3 µs. The origin of the monotonically decreasing component of the spectrum is unclear up to now. Since the amplitude of this component influences the afterpulse probability significantly, no mean value can be given with an adequate uncertainty. The measured values, which lie between 2 % and 10 %, should rather be interpreted as upper limits. The R11410 specifications, which state that the afterpulse probability is less than 10% when measuring between 0 µs and 2 µs, can therefore be confirmed.

3.4 Discussion of experimental test results

The SPE characteristics of the R11410-21 PMTs are very good. A small SPE resolution is important because it enters into the analysis calculating the expected WIMP signal spectrum $f(S1)$ from a given WIMP mass and cross section (and astrophysical parameters) [47]. The peak to valley ratio is $^P/_V = 3.2 \pm 0.4$ and the SPE resolution is $R = (30 \pm 1)\,\%$ at the planned XENON1T operating gain of $2 \cdot 10^6$. This is a clear improvement compared to the XENON100 PMTs, which had $P/V \approx 2$ and $R \approx 50\,\%$ at the same operating gain. Therefore, it is no problem that the gain of the R11410-21 PMTs is only $3.7 \cdot 10^6$ at 1500 V instead of the promised $5 \cdot 10^6$. Note that the PMT body is held at the negative potential corresponding to

the operating voltage. Therefore, the spread of operating voltages should be as low as possible to keep the potential differences between the PMTs low. But the gain variations are small enough so that the needed operating voltages for a gain of $2 \cdot 10^6$ vary by a standard deviation of 50 V around the mean value of 1400 V. Given the spacing of 4 cm between two PMTs, this corresponds to an electric field of about $13\,\mathrm{V\,cm^{-1}}$ which is small compared to the drift field of $10^3\,\mathrm{V\,cm^{-1}}$ for example.

If the PMTs which are producing light can be rejected, the dark count rates of the XENON1T PMTs should have values around 40 Hz. The problem with dark counts is that they can happen simultaneously in two PMTs and mimic an $S1$ signal. The rate of accidental coincidences is equal to the product of the coincidence window, the square of the dark count rate and the number of possible PMT pairs

$$\sum_{i=1}^{N-1} i = \frac{1}{2}(N^2 - N) = 30628 \tag{3.10}$$

for $N = 248$ PMTs. For a coincidence window of 20 ns like in XENON100, the rate of accidental coincidences in XENON1T would be 1 Hz. This seems very large, but one has to keep in mind that such an $S1$ signal has to survive all cuts to be able to be counted as a WIMP event. For example, there must be an $S2$ signal within the right time distance range, the ratio $S1/S2$ must fit etc. For XENON100 with $N = 178$ PMTs and dark count rates of the same size it was estimated that 0.45 accidental coincidence events in 225 days contribute to the WIMP background [22]. Compared to an overall amount of two measured events in the WIMP region [56], this is a significant background. Due to the enhanced number of PMTs in XENON1T the number of accidental coincidence events will increase by a factor of two compared to XENON100.

The rate of accidental coincidences resulting from afterpulses should be larger than the one resulting from dark counts, because afterpulses are time-correlated to main pulses. Thus, after two PMTs have detected photons caused by an event in the LXe, the probability for accidental coincidences at the afterpulse times after the main pulses is enhanced. But since the afterpulse times are known, it might be possible to identify these events containing two $S1$ pulses without the need to reject them.

The coincidence window for the simultaneous detection of two PMT signals has to take into account that the distribution of PMT pulses in time is smeared by several factors: the decay time of LXe scintillation light, which is ≈ 20 ns for the slow component [48], the transit time spread and the sampling rate for the digitization of pulses. In XENON100 the sampling rate is 10 ns and the PMTs have a transit time spread of 1 ns. By all these factors the coincidence window of 20 ns was motivated. In the last section it was presented that the transit time spread of the R11410-21 PMTs is 8 ns on average. Therefore, it might be necessary to use a larger coincidence window than ≈ 20 ns in XENON1T, which will again enahnce the amount of accidental coincidences.

Since the time difference between the $S1$ and $S2$ signals gives the z-position of an interaction within the TPC, one might ask the question if the z-resolution is affected by the transit time spread. The $S1$ and $S2$ signals are composed of the output of several PMTs and in XENON100 both have a typical width of the order of 10 to 100 ns and 1 µs, respectively. In XENON1T the $S2$ pulse width should be even larger because of the larger drift length of the electrons. The main argument is that the electron drift time is of the order of 100 µs and therefore much longer than the TTS. Thus, even in case of a sharp $S1$ pulse the TTS should not be able to affect the z-resolution.

Chapter 4

Light collection simulations for XENON1T

In this chapter, the motivation for simulating the light propagation and collection in XENON1T will be given at first. In the second section, the geometry of the simulated XENON1T-like detector will be described. Afterwards, the simulation results will be presented and discussed.

4.1 Motivation

Simulations of the scintillation light propagation and the light collection efficiency are an important component of XENON1T to be carried out before the construction of the experiment, because the results can be used for an optimization of the detector design. When all photomultiplier tubes have been tested, they will be mounted into a support structure, which will be inserted into the TPC afterwards. But it remains the important question of how to arrange them. In section 1.2 it was explained that the quantum efficiency (QE) of the PMTs significantly influences the light collection efficiency of the detector. But the quantum efficiency values of the PMTs differ because the thickness of the vapor-deposited photocathode is subject to statistical fluctuations. So how does the arrangement of the PMTs within the support structure affect the LCE? This question will be addressed in the chapter at hand.

A high LCE is extremely desirable because it results in a high light yield. This is again important for a lowest possible energy threshold of the detector. Recall that the higher the light yield is, the more $S1$ photons are detected i.e. the more PE are produced, per keV of deposited energy. Thus, the LY enters into the conversion of an $S1$ signal amplitude threshold ($S_1^{\min}$) to a lower limit on deposited recoil energies that can be detected:

$$E^{\min} \propto \frac{S_1^{\min}}{LY} \propto \frac{S_1^{\min}}{LCE}. \tag{4.1}$$

The second proportionality uses Equation 1.2.

The importance of a low energy threshold can be explained by means of Fig. 1.3. The sensitivity of a direct detection experiment is related to the integral of the differential event rate over the recoil energy, starting at the energy threshold. Fig. 1.3 showed, that for WIMPs with lower masses, a steeper falling exponential curve is expected. Therefore, for the detection of light WIMPs, a lower energy threshold is especially important, because the gain in sensitivity is larger than for for heavier WIMPs. In addition, the lower the energy threshold is, the lower the mass of detectable WIMPs can be.

In Fig. 4.1 the distribution of QE values of 60 R11410-21 PMTs is shown. The considered fraction of the PMT production has a mean QE value of 36.9%. Inserting this data into an

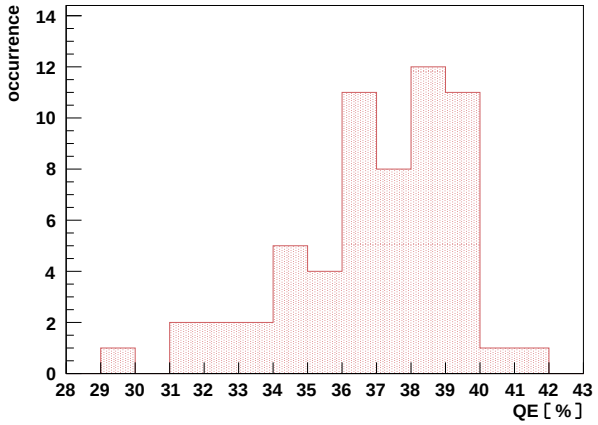

Figure 4.1: *Distribution of QE values of 60 R11410-21 PMTs.*

implementation of a XENON1T-like detector and simulating the emergence and detection of scintillation photons, one can investigate the dependency of the LCE on the distribution of QE values among the PMT positions in the detector.

4.2 The geometry of the simulated detector

A simplified version of the XENON1T detector was implemented by means of the simulation toolkit GEANT4 [49], which is using Monte Carlo methods. Parts of the already existing XENON1T simulation code were adapted [22]. First of all, a cylindric container with Teflon walls and with liquid and gaseous xenon inside was created. It is 120 cm high and has a radius of 52 cm, which is similar to the XENON1T dimensions. Fig. 4.2 shows a cross section through the detector.

Just like the scintillation photons in the real detector, the simulated photons will start at a random position in the liquid xenon volume. Afterwards they can undergo different processes:

- refraction to GXe or Teflon
- absorption by LXe, GXe or Teflon
- Rayleigh scattering in LXe or GXe.
- reflection by Teflon or at the LXe/GXe surface

To enable these processes, one needs to assign values for the absorption length, the Rayleigh scattering length, and the refractive index to all materials (see Table 4.1). To detect the photons, 248 PMTs are implemented like they will be positioned in XENON1T (see Fig. 4.3). The bottom PMTs are arranged aiming to achieve the highest possible density, whereas the top PMTs are arranged in circles, which is an advantage for the spacial reconstruction of an event. The implemented PMTs consist of three parts, visible in the closeup image in Fig. 4.2: a casing, made from kovar (implemented as an alloy consisting of Fe, Ni, Co, C, Si, Mn [22]), a window made from quartz and a metal photocathode, which is located inside of the PMT,

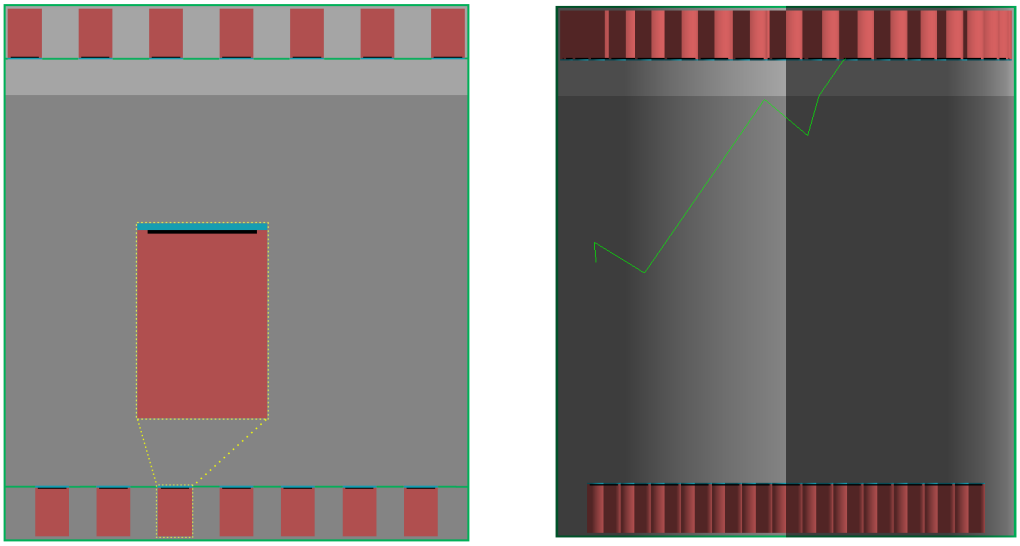

Figure 4.2: *Left: Cross section through the GEANT4 detector. A cylinder consisting of liquid xenon (dark gray) and gaseous xenon (light gray) is surrounded by Teflon walls (green). The PMT arrays are located on the top and on the bottom of the detector. A zoomed in picture of a PMT shows its three components: casing (red), window (blue) and photocathode (black). Teflon reflectors shield the space between the PMTs. Right: Side view on the detector with the front Teflon wall being transparent. The path of a photon, which was scattered several times before it reached a PMT, is shown in green. The shadows are caused by a visualization effect.*

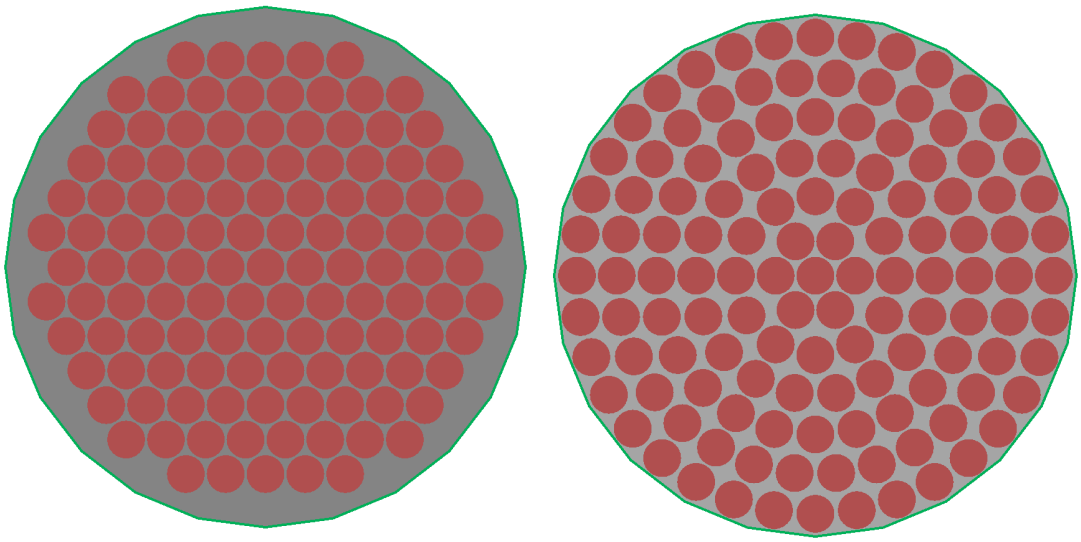

Figure 4.3: *Geometry of the PMT arrangement in the simulated detector like in XENON1T. Left: 121 PMTS in the bottom array, arranged in rows. Right: 127 PMTs in the top array, arranged in circles.*

next to the window. Refractive indices are given to this materials as well and each PMT is assigned a QE value. When a photon hits a PMT window, it is either reflected or transmitted. In the latter case, it can reach the casing or the photocathode. If the photon hits the PMT casing it is absorbed immediately, but when it reaches the photocathode, the decision if the photon is detected or not is made in the following way. A random number between 0 and 1 is generated. If this number is smaller or equal to the quantum efficiency of the PMT that was hit, the photon is detected. If it is larger than QE value, it is not detected. The photon track ends at this point. Note that the correct quantity to insert into the simulation would not be QE from Equation 2.1 but η, because the reflection and absorption is already accounted for by GEANT4. But since only the QE values are available and the difference between QE and η is just a constant factor for all PMTs, the usage of QE has an impact only on the absolute LCE value, which does not affect the aspired result of this study. In addition, to get the absolute LCE value the collection efficiency α would have to be included, but it is left out for the same reason. Fig. 4.2 also shows a Teflon reflector, filling the space between the PMT windows, like there will be in XENON1T. It was introduced so that less photons hit a PMT body, which reduces the number of absorbed and thus lost photons.

The optical properties of all implemented materials are listed in Table 4.1. The absorption

material	n	l_a	l_s
LXe	1.61	100 cm	30 cm [50]
GXe	1.0	100 m	100 m
Teflon	1.35 [51]	1 nm	-
Quartz window	1.59 [52]	30 m [53]	-
Kovar body	-	-	-
Photocathode	1.59	1 nm	-

Table 4.1: *Optical properties of simulated materials. The quantities l_a and l_s are the absorption- and scattering lengths and n is the refractive index.*

length of liquid xenon depends on the level of contamination. It is expected that pure LXe is transparent to its own scintillation light [54] but impurities like water and oxygen, which are dissolved in the xenon, can absorb the scintillation light [50]. The value from Table 4.1 is just a lower limit measured in [54], where xenon with a relative impurity level less than 10^{-9} was used, like in XENON100 [23]. In [50] it is stated that the measured values of the refractive index of LXe ranges from 1.54 to 1.69. The mid-point of this interval is used for the simulation. The refractive index of the implemented photocathode is chosen equal to the one of quartz to avoid reflection and thus loosing photons. The simulated absorption lengths of Teflon and the photocathode are chosen so small because once a photon is transmitted to one of these materials, the photon track should end there. The only other implemented optical property for the Teflon walls is the refractive index. In that case GEANT4 assumes a smooth surface enabling only specular reflection. Analyzing the simulation results, the reflectivity of Teflon is determined to be $\approx 18\,\%$. Actually Teflon has a much more complex surface, resulting in diffuse Lambertian reflectance and allowing for a reflectivity of 95 % at the wavelength of LXe scintillation light [55]. For the discussion of the impact of this deviation, see Chapter 4.4.

The output of the GEANT4 program is a list of events, with the following information for each event: the start position of the photon, if it was detected or not and if yes, which PMT was hit.

4.3 Simulation results

To simulate the xenon scintillation light, photons with random polarization and an energy of 6.98 eV are started in the LXe volume. This energy corresponds to a wavelength of 178 nm, which is the center of the narrow LXe scintillation light emission peak. The start positions are distributed homogeneously and the initial momentum direction is set isotropic.

In a first test, a quantum efficiency of 100 % is assigned to all PMTs. At the end of this section, different QE distributions are tested.

4.3.1 Light collection efficiency map

When N_{det} photons were detected by any PMT after starting N photons in the LXe volume, the light collection efficiency can be defined as

$$LCE = \frac{N_{\mathrm{det}}}{N}. \tag{4.2}$$

In case all PMTs have a quantum efficiency of 100 %, the result for the above described test detector is $LCE = (7.366 \pm 0.002)\,\%$. This is a mean value of $n = 5$ simulations with $N = 10^7$ photons. The given error is calculated as $\sigma/\sqrt{n}$, where $\sigma = 0.004$. This standard deviation is assumed in the following for all runs with $N = 10^7$ photons and will be given as uncertainty to a LCE value that was only measured once. Note that the absolute LCE value obtained here cannot give the expected light collection efficiency for XENON1T because the detector geometry is simplified and contains only the relevant components for studying the difference ΔLCE when changing for example the QE assignment to the PMT positions.

A light collection efficiency can also be defined for one volume element in a similar way:

$$LCE(R, Z) = \frac{N_{\mathrm{det}}(R, Z)}{N(R, Z)}, \tag{4.3}$$

where $N(R, Z)$ is the number of started photons in the volume element at the position (R, Z) in cylinder coordinates and $N_{\mathrm{det}}(R, Z)$ the number of those photons that were detected. Of course, this gives a spatial dependence to the LCE which is illustrated by means an LCE map like in Fig. 4.4. It shows that photons which start at the bottom of the LXe volume have the best chance to be detected, because they start close to the PMT array at the bottom. The LCE has the lowest values around $z = 100$ mm and it increases again for larger z due to the short distance to the top PMT array. But due to the reflection at the LXe/GXe surface the LCE is not as large as on the bottom of the TPC. One can also see that the light collection efficiency decreases with increasing radius. This is because for photons starting at the center, the range of initial momentum angles, which lead to the detection of the photon, in case it is not scattered, is larger than for photons starting at the outer parts of the TPC.

4.3.2 Impact of the quantum efficiency distribution on the light collection efficiency

When a QE of 100 % is given to all PMTs, one can investigate which PMT positions are exposed to how many photons. Let us define an efficiency, which is a property of the PMT position, as

$$LCE^i = \frac{N^i_{\mathrm{det}}}{N}, \tag{4.4}$$

where N is again the number of started photons in the whole LXe volume and N^i_{det} is the number of detected photons by the PMT at the position number i. Note that the LCE in this approach is independent of the photon starting positions.

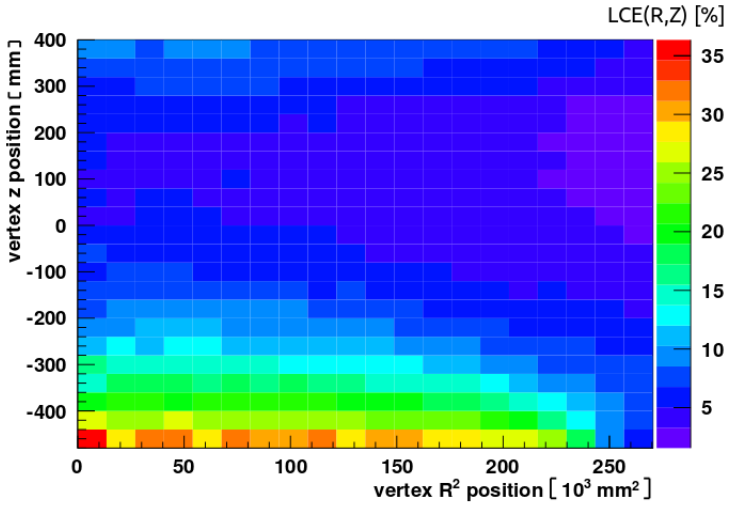

Figure 4.4: *Light collection efficiency map produced with $N = 10^7$ photons. The vertex position is the point where the photon started. The quadratic R axis is chosen because the volume increases quadratically with radius.*

First, the bottom PMT array will be compared to the top array. Fig. 4.5 shows a histogram of the efficiencies of the bottom and top PMTs separately. It reveals that one PMT in the

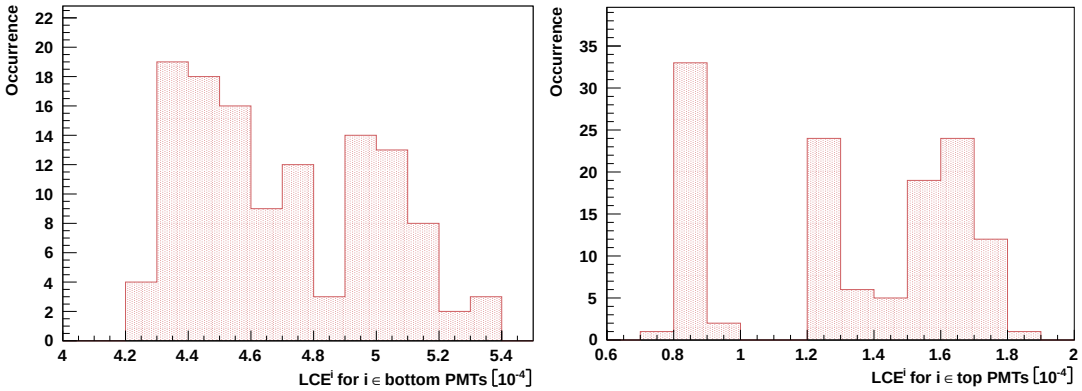

Figure 4.5: *Comparison of bottom (left) and top (right) PMT array efficiency. One can see discrete peaks for the top PMT efficiencies due to the radial arrangement of the PMTs.*

bottom array detects on average 0.47 ‰ of the started photons, whereas a PMT in the top array detects 0.13 ‰ on average and each bottom PMT is more efficient than any top PMT. Because the photons start in liquid xenon and they undergo total internal reflection at the GXe surface in case the incident angle, with respect to the normal, is larger than

$$\theta_c = \arcsin\left(\frac{n_{\mathrm{GXe}}}{n_{\mathrm{LXe}}}\right) = 38^\circ, \tag{4.5}$$

77 % of the photons are detected by bottom PMTs and 23 % by the top PMTs. In XENON100, about 80 % of the photons are detected by the PMTs in the bottom array [23].

Any position dependency of the efficiency within the two groups (bottom and top) can only be radial nature due to the cylinder symmetry of the detector. In Fig. 4.6 the efficiency

of a PMT position is shown as a function of its radius, i.e. the distance from the symmetry axis of the detector. It shows that the efficiency decreases with radius. The reason for this

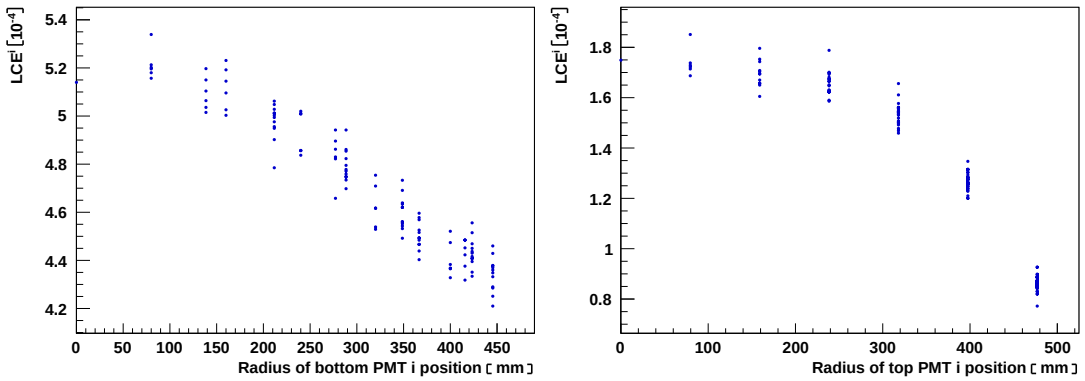

Figure 4.6: *Radial dependency of the PMT position efficiency. Left: bottom PMT array. Right: top PMT array. The different shapes of the two curves are due to different reflection properties of the surfaces LXe/Teflon and GXe/Teflon.*

effect is that the Teflon walls do not reflect all photons and therefore the outer PMTs have a smaller range of solid angles for incoming photons.

Now, the aforementioned results can determine the arrangement of QE values amongst the PMT positions to achieve the maximum possible LCE. In the following, the 60 actual QE values shown in Fig. 4.1 are used. Since 248 PMTs have to be assigned with a quantum efficiency, each value is used 4 times and the mean value of 36.9 % is used for the eight remaining PMTs. Afterwards, the QE values are sorted. The best-case scenario would be placing the PMTs with the highest QE in the middle of the bottom array, sorting the quantum efficiencies according to the PMT position efficiencies radially outwards and continuing with the top PMT array in the same way. The worst-case scenario is arranging the PMTs the other way round, i.e. placing the highest QE values at the outer edge of the top array and the lowest QE value in the middle of the bottom array. These two cases were simulated and the LCE was calculated for both. The results are $LCE = (2.806 \pm 0.004)\,\%$ in the best case and $LCE = (2,628 \pm 0.004)\,\%$ in the worst case. A random PMT distribution would yield a light collection efficiency between these two values. Therefore, $(6.8 \pm 0.2)\,\%$ of the LCE value can be gained at most, when the arrangement of the PMTs is optimized.

4.4 Discussion of simulation results

For XENON100 the $S1$ threshold could be set to 3 PE [56] which means that only $S1$ signals, which are larger than 3 PE are retained. This value was motivated in the following way: The threshold for a single PMT signal was set to 0.3 PE. Considering the coincidence condition, which states that at least two PMTs must respond simultaneously, the threshold for a valid signal would be 0.6 PE. But one has to keep in mind that the acceptance, i.e. the percentage of "good" events which is accepted by a cut, decreases with decreasing energy for some cuts like the coincidence condition for example, while the uncertainty of the acceptance increases due to low statistics. This compromise between the possibility to detect low energies on the one hand and small uncertainties in the analysis on the other hand, determines the energy threshold for nuclear recoils. It was set to 6.6 keV in XENON100 [56]. Gaining 6.8 % in LCE results in the light yield increasing by 6.8 %, too, because the quantity ξ in Equation 1.2 is a constant

property of the liquid xenon. Using Equation 4.1, a 6.8 % higher LY only approximately leads to a 6.8 % lower energy threshold, because the proportionality factor of the first relation in Equation 4.1, which includes L_{eff}, is energy dependent.

One might ask if it is really desirable to maximize the LCE when the prize is making the detector more inhomogeneous. Sorting the PMTs like it described above, enhances the probability for light to be detected at efficient positions but even makes it more unlikely that light is detected at PMT positions with lower efficiencies. This might be a disadvantage for the reconstruction of the x- and y-position reconstruction which uses the PMT hit pattern of the top PMT array. But since the quantum efficiencies of all PMTs are known, the position reconstruction can take them into account and correct the signals.

Fig. 1.5 shows the electrode meshes that are an essential part of the TPC, but which were left out in this simulation. The presence of the meshes only changes the absolute LCE value but it should make no difference for the result presented above, because their structure is homogeneous over the cross section of the TPC. Many other components of the TPC from outside the active volume are omitted, too, which makes no difference either.

One factor that will affect the result of the simulation described in Chapter 4 is the reflectivity of Teflon. It is lower for the implemented Teflon than for the real material. It is plausible that a higher reflectivity might flatten the function describing the efficiency versus radius of the PMT position shown in Fig. 4.6. This would make the PMT sorting more ineffective. Therefore, the presented results must be interpreted as a first approach to this task. Another source of error are the parameters listed in Table 4.1, but the impact of their uncertainties should be negligible compared to the effect of an enhanced Teflon reflectivity.

Chapter 5

Summary and outlook

After XENON100 has set world-leading limits on the WIMP nucleon cross section, the goal of the successor experiment XENON1T is to improve the sensitivity by 2 orders of magnitude. To achieve this, in addition to increasing the target volume by a factor of 10, the background events have to be reduced by 2 orders of magnitude. Employing the new Hamamatsu R11410-21 PMT, which was developed to have an ultra low intrinsic radioactivity for XENON1T, is a necessary step towards this goal. It also features a very high quantum efficiency of typically 32.5 %, which is also an improvement compared to the XENON100 PMTs, and which will contribute to a higher light yield and thus a lower energy threshold of the experiment, enhancing the sensitivity especially for low WIMP masses.

In this thesis, the performance of the R11410-21 PMT was investigated. Using the described MPIK setups, 90 of 250 PMTs have been tested for compatibility with the experiments requirements. Important PMT features were measured at room and LXe temperature and every PMT passed the thermal stress test of 3 cool-down cycles. An optimal operating gain of $2 \cdot 10^6$ in terms of a maximal peak to valley ratio of $\overline{P/V} = 3.2 \pm 0.4$, a maximal SPE resolution of $\overline{R} = (30 \pm 1)\,\%$ at a minimal operating voltage of $\overline{U} = (1400 \pm 50)\,\mathrm{V}$ was found. Even if some PMTs had to be replaced due to enhanced or unstable dark count rates, most PMTs have a very low dark count rate of around 40 Hz at $-100\,^{\circ}\mathrm{C}$ and the afterpulse probability of all PMTs does not exceed 10 %. Overall, it can be confirmed that all important requirements of the experiment XENON1T are met by the first 90 of PMTs. Further 160 PMTs will be tested by the beginning of 2015. Afterwards, all 250 PMTs will be installed into the dedicated support structure, which will be mounted into the TPC afterwards.

The second part of this thesis is devoted to developing an LCE-optimized PMT distribution across the already fixed positions in the support structure, with respect to the quantum efficiencies of the PMTs. For this purpose, the light collection efficiencies of the individual PMT positions, given by the detector geometry, were investigated. It was found that all positions in the bottom array PMT are more efficient than those in the top array and within one array, the efficiency decreases with increasing distance to the symmetry axis of the detector. Now, the optimized PMT arrangement can be achieved by sorting the PMTs with respect to their quantum efficiencies and assigning the PMT with the highest QE to the most efficient PMT position etc. In a first approach, it was shown that the XENON1T light collection efficiency can be enhanced by a factor of $(6.8 \pm 0.2)\,\%$ at most by using the described arrangement. Therefore, the light yield can be enhanced and the energy threshold can be lowered approximately by this percentage. As a next step, the present LCE simulation has to be extended to include more realistic reflection properties of Teflon to check if the effect of significantly decreasing PMT position efficiency with increasing radius stays valid.

XENON1T will start commissioning in 2015 and will be able test a completely new area of WIMP-nucleon cross sections by 2017.

Appendix A

Additional information

name	value
$\tilde{U}_0$	gain $3 \cdot 10^6$
$\tilde{U}_1$	gain $2 \cdot 10^6$
HV2	1320 V
HV3	1380 V
HV4	1440 V
HV5	1500 V
HV6	1540 V
HV7	1580 V
HV8	1640 V
HV9	1680 V

Table A.1: *Operating voltage abbreviations.*

List of Figures

List of Tables

Bibliography

[1] J. Oort, "The force exerted by the stellar system in the direction perpendicular to the galactic plane and some related problems," *Bull. Astron. Inst. Neth.* **6** (1932) 249.

[2] F. Zwicky, "Die Rotverschiebung von extragalaktischen Nebeln," *Helv. Phys. Acta* **6** (1933) 110.

[3] V. C. Rubin, N. Thonnard, and W. K. Ford, "Extended rotation curves of high-luminosity spiral galaxies," *Astrophys. J.* **225** (1978) L107.

[4] K. G. Begeman, A. H. Broeils, and R. Sanders, "Extended rotation curves of spiral galaxies - dark haloes and modified dynamics.," *Mon. Not. R. Astron. Soc.* **249** (1991) 523–537.

[5] M. Milgrom, "A modification of the newtonian dynamics as a possible alternative to the hidden mass hypothesis," *Astrophys. J.* **270** (1983) 365.

[6] G. Bertone, *Particle Dark Matter. Observations, Models and Searches.* Cambridge University Press, 2010.

[7] M. Markevitch, A. Gonzalez, L. David, A. Vikhlinin, S. Murray, *et al.*, "A textbook example of a bow shock in the merging galaxy cluster 1E0657-56." arXiv:astro-ph/0110468, 2002.

[8] M. Markevitch, A. H. Gonzalez, D. Clowe, A. Vikhlinin, W. Forman, *et al.*, "Direct constraints on the dark matter self-interaction cross section from the merging galaxy cluster 1E0657-56," *Astrophys. J.* **606** (2004) 819.

[9] http://chandra.harvard.edu/.

[10] D. Clowe, M. Bradač, A. H. Gonzalez, M. Markevitch, S. W. Randall, *et al.*, "A direct empirical proof of the existence of dark matter," *Astrophys. J.* **648** (2006) L109.

[11] K.Griest, "Galactic microlensing as a method of detecting massive compact halo objects," *Astrophys. J.* **366** (1991) 412–421.

[12] C. Alcock et al. (MACHO Collaboration), "The MACHO project: Limits on planetary mass dark matter in the galactic halo from gravitational microlensing," *Astrophys. J.* **471** (1996) 774.

[13] G. Jungman, M. Kamionkowski, and K. Griest, "Supersymmetric dark matter," *Phys. Rep.* **267** (1996) 195.

[14] V. Springel, C. S. Frenk, and S. D. M. White, "The large-scale structure of the universe," *Nature* **440** (2006) 1137.

[15] P.A.R. Ade et al. (Planck Collaboration), "Planck 2013 results. I. overview of products and scientific results." arXiv:1303.5062 [astro-ph.CO], 2013.

[16] M. Schumann, "Dark matter 2013." arXiv:1310.5217 [astro-ph.CO], 2013.

[17] M. Goodman and E. Witten, "Detectability of certain dark matter candidates," *Phys. Rev. D* **31** (1985) 3059.

[18] A. K. Drukier, K. Freese, and D. N. Spergel, "Detecting cold dark-matter candidates," *Phys. Rev. D* **33** (1986) 3495.

[19] R. Bernabei, P. Belli, F. Cappella, R. Cerulli, C. Dai, *et al.*, "First results from DAMA/LIBRA and the combined results with DAMA/NaI," *Eur. Phys. J. C* **56** (2008) 333.

[20] R. Bernabei, P. Belli, F. Cappella, R. Cerulli, C. Dai, *et al.*, "Final model independent result of DAMA/LIBRA phase1," *Eur. Phys. J. C* **73** (2013) 12.

[21] C. E. Aalseth et al. (CoGeNT Collaboration), "Search for an annual modulation in a p-type point contact germanium dark matter detector," *Phys. Rev. Lett.* **107** (2011) 141301.

[22] XENON collaboration. Personal communication.

[23] E. Aprile et al. (XENON100 Collaboration), "The XENON100 dark matter experiment," *Astropart. Phys.* **35** (2012) 573–590.

[24] D. McKinsey, D. Akerib, S. Bedikian, A. Bernstein, A. Bolozdynya, *et al.*, "The LUX dark matter search," *J. Phys. Conf. Ser.* **203** (2010) 012026.

[25] http://www.lngs.infn.it/.

[26] Z. Ahmet et al. (CDMS II Collaboration), "Dark matter search results from the CDMS II experiment," *Science* **327** (2010) 1619–1621.

[27] G. Angloher, M. Bauer, I. Bavykina, A. Bento, C. Bucci, *et al.*, "Results from 730 kgdays of the CRESST-II dark matter search," *Eur. Phys. J. C* **72** (2012) 1971.

[28] V. Sanglard et al. (EDELWEISS Collaboration), "Final results of the EDELWEISS-I dark matter search with cryogenic heat-and-ionization Ge detectors," *Phys. Rev. D* **71** (2005) 122002.

[29] R. Agnese et al. (CDMS Collaboration), "Silicon detector dark matter results from the final exposure of CDMS II," *Phys. Rev. Lett.* **111** (2013) 251301.

[30] R. Agnese, A. Anderson, M. Asai, D. Balakishiyeva, R. B. Thakur, *et al.*, "Search for low-mass WIMPs with SuperCDMS." arXiv:1402.7137 [hep-ex], 2014.

[31] E. Aprile, "The XENON1T dark matter search experiment," in *Sources and Detection of Dark Matter and Dark Energy in the Universe*, pp. 93–96. Springer, 2013.

[32] A. Lansiart, A. Seigneur, J.-L. Moretti, and J.-P. Morucci, "Development research on a highly luminous condensed xenon scintillator," *Nucl. Instrum. Methods* **135** (1976) 4752.

[33] E. Aprile, F. Agostini, M. Alfonsi, K. Arisaka, F. Arneodo, *et al.*, "Conceptual design and simulation of a water cherenkov muon veto for the XENON1T experiment." arXiv:1406.2374 [astro-ph.IM], 2014.

[34] Hamamatsu Photonics K.K., "Photomultiplier tubes: Basics and applications," 2007.

[35] J. Haser, F. Kaether, C. Langbrandtner, M. Lindner, S. Lucht, *et al.*, "Afterpulse measurements of R7081 photomultipliers for the Double Chooz experiment," *J. Instrum.* **8** (2013) P04029.

[36] L. Baudis, A. Behrens, A. Ferella, A. Kish, T. Marrodán Undagoitia, *et al.*, "Performance of the hamamatsu R11410 photomultiplier tube in cryogenic xenon environments," *J. Instrum.* **8** (2013) P04026.

[37] K. Lung, K. Arisaka, A. Bargetzi, P. Beltrame, A. Cahill, *et al.*, "Characterization of the hamamatsu R11410-10 3-in. photomultiplier tube for liquid xenon dark matter direct detection experiments," *Nucl. Instrum. Methods A* **696** (2012) 32 – 39.

[38] XENON Collaboration. to be published.

[39] L. Baudis, A. Ferella, A. Askin, J. Angle, E. Aprile, *et al.*, "Gator: a low-background counting facility at the gran sasso underground laboratory," *J. Instrum.* **6** (2011) P08010.

[40] D. Budjáš, W. Hampel, M. Heisel, G. Heusser, M. Keillor, *et al.*, "Highly sensitive gamma-spectrometers of GERDA for material screening." arXiv:0812.0768 [physics.ins-det], 2008.

[41] A. Behrens, *Light Detectors for the XENON100 and XENON1T Dark Matter Search Experiments*. PhD thesis, Mathematisch-naturwissenschaftliche Fakultät der Universität Zürich, 2014.

[42] F. Kaether. Personal communication.

[43] D. Cichon, "Examining hamamatsu R11410-21 photomultipliers for XENON1T at room and liquid xenon temperatures." Bachelor's thesis, department of physics and astronomy, Ruprecht-Karls-Universität Heidelberg, 2013.

[44] C. Bauer, E. Borger, R. Hofacker, K. Jänner, F. Kaether, *et al.*, "Qualification tests of 474 photomultiplier tubes for the inner detector of the Double Chooz experiment," *J. Instrum.* **6** (2011) P06008.

[45] F. Kaether *et al.*, "PMT testing at MPIK." Talk at Double Chooz meeting, Kobe, 2008.

[46] F. Kaether and C. Langbrandtner, "Transit time and charge correlations of single photoelectron events in R7081 photomultiplier tubes," *J. Instrum.* **7** (2012) P09002.

[47] E. Aprile et al. (XENON100 Collaboration) , "Likelihood approach to the first dark matter results from XENON100," *Phys. Rev. D* **84** (2011) 052003.

[48] T. Doke and K. Masuda, "Present status of liquid rare gas scintillation detectors and their new application to gamma-ray calorimeters," *Nucl. Instrum. Methods A* **420** (1999) 62–80.

[49] S. Agostinelli, J. Allison, K. Amako, J. Apostolakis, H. Araujo, *et al.*, "GEANT4 - a simulation toolkit," *Nucl. Instrum. Methods A* **506** (2003) 250303.

[50] E. Aprile and T. Doke, "Liquid xenon detectors for particle physics and astrophysics," *Rev. Mod. Phys.* **82** (2010) 2053.

[51] M. K. Yang, E. W. Tokarsky, and R. H. French, "Optical properties of Teflon AF amorphous fluoropolymers," *J. Micro Nanolithogr. MEMS MOEMS* **7** (2008) 033010.

[52] D. Akerib, X. Bai, S. Bedikian, E. Bernard, A. Bernstein, *et al.*, "LUXSim: A component-centric approach to low-background simulations," *Nucl. Instrum. Methods A* **675** (2012) 6377.

[53] R. Kitamura, L. Pilon, and M. Jonasz, "Optical constants of silica glass from extreme ultraviolet to far infrared at near room temperature," *Appl. Opt.* **46** (2007) 8118–8133.

[54] A. Baldini, C. Bemporad, F. Cei, T. Doke, M. Grassi, *et al.*, "Absorption of scintillation light in a 100 l liquid xenon gamma-ray detector and expected detector performance," *Nucl. Instrum. Methods A* **545** (2005) 753764.

[55] M. Yamashita, T. Doke, K. Kawasaki, J. Kikuchi, and S. Suzuki, "Scintillation response of liquid Xe surrounded by PTFE reflector for gamma rays," *Nucl. Instrum. Methods A* **535** (2004) 692698.

[56] E. Aprile et al. (XENON100 Collaboration), "Dark matter results from 225 live days of XENON100 data," *Phys. Rev. Lett.* **109** (2012) 181301.

Erklärung:

Ich versichere, dass ich diese Arbeit selbstständig verfasst habe und keine anderen als die angegebenen Quellen und Hilfsmittel benutzt habe.

Heidelberg, den (Datum) .....

Danksagung

Zunächst möchte ich mich bei Prof. Manfred Lindner dafür bedanken, dass er mich in seine Arbeitsgruppe aufgenommen hat und mir somit die Möglichkeit gegeben hat, in dieser spannenden Phase des XENON Projektes dabei sein zu dürfen.
Mein Dank gilt außerdem Prof. André Schöning dafür, dass er sich dazu bereiterklärt hat, die Zweitbegutachtung dieser Arbeit zu übernehmen.
Besonders möchte ich Dr. Teresa Marrodan und Dr. Florian Kaether dafür danken, dass sie mir alle meine Fragen mit Freude und Engagement beantwortet haben und mir jederzeit mit Rat und Tat zur Seite standen. Ihre motivierende Art hat entscheidend dazu beigetragen, dass ich im letztem Jahr viel gelernt habe.
Mein Dank gilt auch Dominick Cichon, da er mich in meinen ersten Wochen am MPI so gut in die tägliche Arbeit im Faraday Labor eingearbeitet hat.
Der ganzen Arbeitsgruppe bin ich dankbar für die freundschaftliche Atmosphäre und die Hilfsbereitschaft, die mit dazu beigetragen haben dass ich stets gerne ans Institut gegangen bin, auch wenn es mit der Arbeit mal nicht so gut lief.
Nicht unerwähnt bleiben soll Marc Weber, der mir geholfen hat einen Einstieg in die Arbeit mit GEANT4 zu finden. Insbesondere der GEANT4-Workshop, den er für alle Interessierten organisiert und abgehalten hat war sehr lehrreich.
Allen Korrekturlesern danke ich natürlich besonders für das gründliche Lesen und die hilfreichen Verbesserungsvorschläge.
Schließlich möchte ich noch meinen Eltern und meinem Freund Alex für ihre bedingungslose Unterstützung danken.